Response to the Editor of the manuscript
" Precipitation downscaling using a probability-matching approach and geostationary infrared data: An evaluation over six climate regions"
by Matthias Bernhardt submitted to Hydrology and Earth System Sciences.

Manuscript Number: hess-2017-592
Revision due before: 16 June 2018

We thank the reviewers and editor for their time in reviewing the manuscript. Those comments are valuable to improve the manuscript. We have considered the comments very carefully and made revisions to the manuscript. Our point-by-point replies to the comments and suggestions are described as below. The responses are marked in blue. The changes made in the revised manuscript are marked in red.

Responses to Reviewer 1

Comment 1

p1l11: "proposed" better present tense?

Response:

Thank you for your useful advice. We have revised it. Please see line 11 in page 1 (red color).

Comment 2

p2l2: which challenges and problems?

Response:

Thank you for your very valuable and careful advice. These problems mean advantages of gauge data and RADAR. We think the description “These problems can be effectively resolved by using satellite remote sensing techniques” may not make logical sense. Thus, we removed this sentence, which will not result in inconsistency of the context.

The main problem is no dense and high-quality gauge network to evaluate RADAR data. Because RADAR has high resolution, there is always no gauge located within the pixel. It is difficult to get the answer how good are RADAR estimates and its full structure of the error distribution.

Comment 3

fig1: c is unclear what can be seen there

Response:

Thank you for your useful advice. We have revised it. Please see figure 2.

Comment 4

p3l19ff: the matching is not decribed, what means matching how is it done? Formula? Is that Quantile mapping?

Response:

Thank you for your very valuable advice. It is very significant to improve our paper. CDF matching belongs to quantile mapping. CDF matching relates one variable (Tb in our study) to reference (precipitation in our study) using same cumulative frequency. We used figure and formula to explain the CDF matching.

Specifically, the matching process is shown as figure 2 (Reference represents precipitation rate; variable represents Tb). The matching process is implemented by a one-to-one mapping CDF of variable onto that of the reference (Equation 5). We have added the description of the CDF matching in the manuscript and equation 5, and revised figure 2. Please see line 5~6 in page 5 (red color) and figure 2.

The matching process of Tb and CMORPH is decripted in line 11~15 in page 6 (red color).

Thanks again for your valuable advice.

Comment 5

p4l11: ..behind [the] downscaling.

Response:

Thank you for your useful advice. It has been revised. Please see line 25 in page 5 (red color).

Comment 6

p4l28ff: sentence is unclear, what is a non-raining frequency?

Response:

Thank you for your very valuable advice. It is very significant to improve our paper. “a non-raining frequency” is an unclear expression. Here, it means the frequency of critical value of rain rate when rain rate is less than the value, it would not rain. As shown in figure below, the rain–no-rain threshold is set at about v_i where the cumulative frequency equals C_i.

Specially, all precipitation rate (Tb) are sorted in ascending (descending) order. Then cumulative probability distributions are both obtained. The cumulative probability is defined as critical probability

when precipitation rate equals zero. The rain-no-rain threshold is the Tb with cumulative probability same as the critical probability. As shown in Fig. 2c and 2d (T means precipitation rate; V represents Tb), the rain–no-rain threshold is set at about v_i where the cumulative probability equals C_i (critical probability).Please see line 11~15 in page 6 (red color).
Thanks again for your valuable advice.

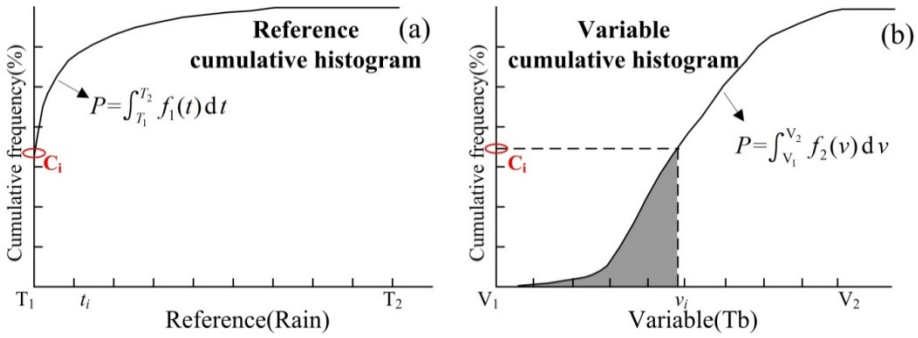

Comment 7
p5l20 and p6l2: A variogram
Response:
Thank you for your useful advice. We have revised them. Please see line 8 and line 9 in page 7 (red color).

Comment 8
p5l21: (Matheron,..)
Response:
Thank you for your useful advice. We have revised it. Please see line 9 in page 7 (red color).

Comment 9
Chapter 2.3 and 2.4 also fig 3, tab.1 are well known scores and techniques maybe you skip them.
Response:
Thank you for your useful advice. We have removed chapter 2.3, also fig 3 (Schematic of the variogram curve), tab.1 (Contingency table for the definition of the categorical metrics).

Comment 10

Fig4: please exclude the islands with climate situations 8 and 9 from the map. The status of these territories are unclear.

Response:

We used the distribution of average annual precipitation during 1960~2010 as base map because it is an most important factor for selecting evaluation regions. Please see figure 1.

Comment 11

Fig5: is again a processing scheme, maybe it is better to make one out of fig2 and fig5, if you change the order of chapter 2 and 3 you can combine chapters 3.3 and 2.2

Response:

Thank you for your so careful and valuable advice. We agreed with you. New figure 3 was made combing fig2 and fig5. We have changed the order of chapter 2 and 3. We first introduced study areas and datasets (chapter 2), and then the methodology (chapter 3). We have combined chapter 3.3 and 2.2 into 3.2.

Comment 12

p7: I found to0 much information in chapter 3.2.2 maybe you short it and only refer to the 2 or 3 most important references.

Response:

Thank you for your useful advice. We agreed with you. We have removed some redundant description. We think these description are better in discussions. Please see line 3~9 in page 10 (red color).

Comment 13

p8l15: [the] image ....definitely needs language editing

Response:

Thank you for your so careful and useful advice. We have revised the description. Please see line 4~6 in page 7 (red color).

Comment 14

fig7: inscribe, which picture is cmorph data and which dcdf, and which picture belongs to which region, maybe confusing or unclear for the reader.

Response:

Thank you for your useful advice. We have revise figure5. Please see fig.5.

Comment 15

p9l7ff: please write sill, range when necessary instead of d and c+c0

Response:

Thank you for your useful advice. We have revised them. Please see line 7, 8 an 15 in page 8 (red color).

Comment 16

p9-10l32ff: Fig 10, according to the shown events the conclusion is not significant, the better fit of dcdf at gauge scale may be pure luck.

Response:

Thank you for your very valuable advice. It is very significant to improve our paper. It is difficult to validate the representativeness of the selected gauge (point) (red dots in figure below) in every region. We just selected these six gauges because their annual precipitation almost equal to average precipitation over area in respective region.

We have compared the DCDF, CMORPH and gauge for all gauges. You are right that not all the fit of DCDF at gauge scale is better than CMORPH. The result showed that the better fit between DCDF and gauge than that between CMORPH and gauge is 10%. The nearly equivalent fit is 69%. The poorer fit is 21%, and mainly happened in region NW, CW and TP.

We have revised the description in our results (Please see line 32 in page 8 and line 1~5 in page 9) (red color), and conclusions (Please see line 23~24 in page 11) (red color).

Thanks again for your valuable advice.

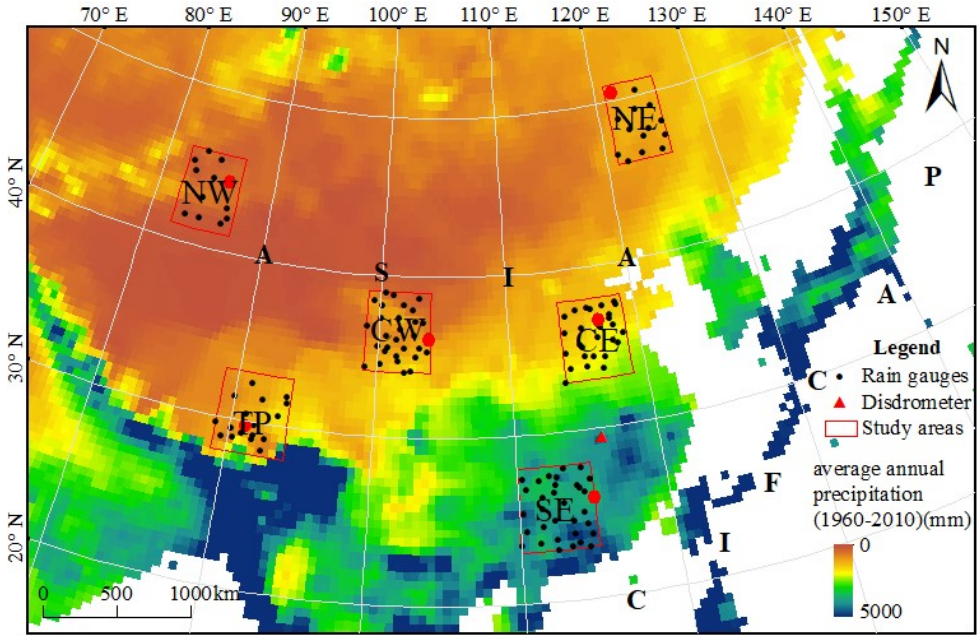

Comment 17

p10l11ff: the bad performance of the approach in winter was something i except reading your methods. How are the correlations between tb and rain in teh winter months?

Response:

The table below gives R^2 in four seasons. The most average of R^2 are higher than 0.90 for six regions in four seasons. The maximum CC is higher than 0.98. Most of the minimum R^2 is higher than 0.80 in summer and autumn. Minimum R^2 ranges from 0.60 to 0.89 in spring, and from 0.51 to 0.71 in winter. It showed that Tb had relatively poor correlation with precipitation rate in winter. This result may inferred that the bad performance of the approach in winter is mainly caused by low accuracy of CMORPH, which may be also applicable for dry regions and mountainous or hilly areas.

Time		SE	CE	NE	CW	NW	TP
SP	Mean	0.91	0.97	0.96	0.98	0.97	0.98
	Max	0.99	0.99	0.99	0.99	0.99	0.99
	Min	**0.64**	0.89	**0.60**	0.83	**0.73**	**0.78**
	Std	0.05	0.02	0.04	0.01	0.02	0.02
SU	Mean	0.92	0.96	0.96	0.97	0.99	0.97
	Max	0.98	0.99	0.99	0.99	0.99	0.99
	Min	0.84	**0.77**	0.85	0.86	0.97	0.86

	Std	0.03	0.03	0.02	0.03	0.00	0.03
FA	Mean	0.97	0.97	0.97	0.97	0.88	0.98
	Max	0.99	0.99	0.99	0.99	0.99	0.99
	Min	0.82	0.89	0.87	0.86	**0.64**	0.94
	Std	0.04	0.03	0.03	0.02	0.11	0.01
WI	Mean	0.92	0.92	0.89	0.95	0.92	0.97
	Max	0.99	0.99	0.99	0.99	0.99	0.99
	Min	**0.65**	**0.51**	**0.60**	**0.71**	**0.58**	**0.69**
	Std	0.07	0.07	0.09	0.04	0.07	0.03

Comment 18

p10l13: rain-no-rain threshold, where is this threshold defined? how large is threshold?

Response:

Thank you for your very valuable advice. I am sorry I didn't explain it clearly. All precipitation rate (Tb) are sorted in ascending (descending) order. Then cumulative probability distributions are both obtained. The cumulative probability is defined as critical probability when precipitation rate equals zero. The rain-no-rain threshold is the Tb with cumulative probability same as the critical probability. As shown in figure below, the rain–no-rain threshold is set at about vi where the cumulative frequency equals Ci. Please see line 11~15 in page 6 (red color).

The threshold generally ranges from 190K to 270K, and most thresholds fall between 200K and 250K. As examples in fig5, the probability of precipitation rate was the largest for a given Tb in region SE, followed by region CE and then region NE. The rain-no-rain thresholds for regions CW and NW were approximately 230 K, while 254K for region TP. The probability of precipitation rate was the largest for a given Tb in region TP.

Thanks again for your valuable advice.

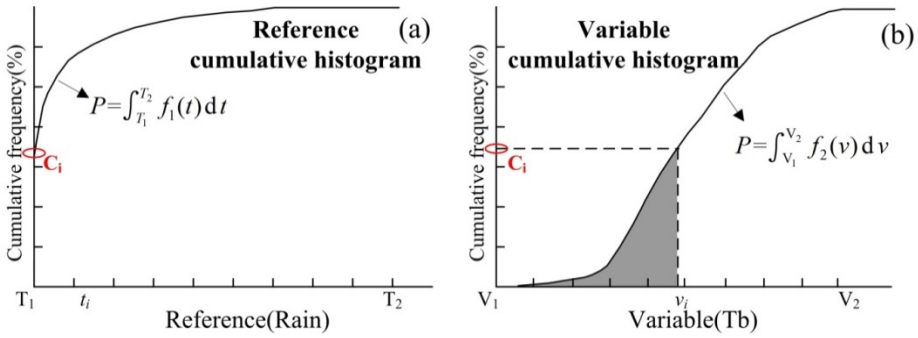

Comment 19

p10l15: what is meant by complex rain systems?

Response:

Thank you for your very helpful advice. I am sorry I didn't describe it exactly. It means orographic rain systems over mountainous or hilly areas. We have revised this sentence. Please see line 16 in page 9 (red color).

Comment 20

p12l3f: I don't agree with that. the method has problems with, heavy rain (cold, tall clouds), with complex rain systems? and in winter.

Response:

Thank you for your very valuable advice. This description is not accurate. We have revised it. The DCDF reflected more detailed moving and changing processes of rainfall under the condition that DCDF perform better than or nearly equivalent to CMORPH. Please see line 17~18 in page 11 (red color).

Responses to Reviewer 2:

The authors proposed a downscaling method based on CDF to obtain hourly 0.05 ° grid precipitation data. This topic is interesting and would be useful for the climate change community. In general, this paper is well-written for most parts. However, a minor revision is needed before it is published in HESS.

Comment 1

Precipitation is more complex to downscaling than temperature. Until now, hundreds of methods have been developed via statistical and dynamical approaches. However, there is none common method for

all regions. The authors did not state clearly about statistical and dynamical downscaling methods in the introduction. The presented study is a statistical downscaling which only used the outputs (CMORPH and GEO-IR) to explore a statistical link. From my side, this approach is similar with Quantile-Mapping (QM), which the authors did not mention. What is the difference between QM and DCDF? The reviewer did not figure out from the Equations (1) to (7).

Response:

Thank you for your very valuable advice. It is very significant to improve our paper. CDF matching belongs to quantile mapping. CDF matching relates one variable (Tb in our study) to reference (precipitation in our study) using same cumulative frequency. We used figure and formula to explain the CDF matching.

The matching process is implemented by a one-to-one mapping CDF of variable onto that of the reference (Eq. 5). We added equation 5. Please see line 5~6 in page 5 (red color).

For matching between Tb and CMORPH, all precipitation rate (Tb) are sorted in ascending (descending) order. Then cumulative probability distributions are both obtained. The cumulative probability is defined as critical probability when precipitation rate equals zero. The rain-no-rain threshold is the Tb with cumulative probability same as the critical probability. Then the CDF matching was applied. All pixels in the Tb images (Tb0.05) were divided into two categories, raining ones less than the rain-no-rain threshold and non-raining ones larger than the threshold. Tb-R relationships were applied to these raining pixels. Finally, CMORPH data were downscaled to 1-hour, 0.05°×0.05°.

Two different approaches are currently being pursued. Dynamical downscaling uses regional climate models (RCMs) to translate the large-scale weather evolution from a GCM into a physically consistent evolution at higher resolution. Statistical downscaling is based on empirical relationships between the regional climate and carefully selected large-scale predictor variables. Please see line 19~22 in page 2 (red color).

Thanks again for your valuable advice.

Comment 2

Is it possible that the information is missing in the process of 0.05 degree data aggregated to 0.25degree? Can the built relationship from a coarse resolution represent the similar features for a higher resolution? What method was used in the aggregation, sum or mean? Does it affect the result?

Response:

Thank you for your very valuable comment. 0.05° Tb was aggregated to 0.25° by arithmetic averaging. Then 0.25° Tb (after aggregation) is matched with CMORPH for raining pixels by quantile-mapping the CDF. Because variability of precipitation cloud is small over 0.25° region, we think the values

(number=25) of 0.05° Tb within a raining pixel are almost the same. That is, the information is to some extent missing in the process of 0.05° data aggregated to 0.25°, but which has a little effect on the Tb-Rain relationship and DCDF result. That is, the built relationship from a coarse resolution generally can represent the similar features for a higher resolution.

We think what method was used in the aggregation would affect the result. If we use the bi-cubic convolution method or bi-linear method, 0.25° Tb after aggregation will involves the information beyond 0.25° pixel. Then it will have effect on the Tb-Rain relationship and DCDF result, and the built relationship from a coarse resolution generally can not represent the similar features for a higher resolution.

In summary, we think arithmetic averaging method is propably best choice.

Comment 3

The structure may be adjusted. I prefer to introduce the data and study area firstly and then followed by the method. The equations for validate criteria are not necessary since they are common used.

Response:

Thank you for your helpful advice. We have changed the order of chapter 2 and 3. We first introduced study areas and datasets (chapter 2), and then the methodology (chapter 3). We have removed dedcription of well known validation index (correlation coefficient (CC), root mean square error (RMSE) and bias, and tab.1).

Comment 4

The authors claimed that DCDF performs better in the frontal rain systems but worse in mountainous. Is CMORPH the main reason for that? If use the reanalysis (e.g. ERA-Interim) for downscaling, will be better? I suggest more discussions on it.

Response:

Thank you for your very valuable advice. We agreed with you. It is very significant to improve our paper. The table below gives R2 in four seasons. The most average of R2 are higher than 0.90 for six regions in four seasons. This result may infer that the bad performance of the approach is mainly caused by low accuracy of CMORPH. Thus using reanalysis data for downscaling may be better than satellite products. Additionally, the assumption of DCDF method is also applied to reanalysis data. It is expected that the DCDF method also applied to reanalysis precipitation data (e.g. ERA-Interim, 0.75°/6 hourly).

We have discussed this issue in the paper. Please see line 13~17 in page 10 (red color).

Time		SE	CE	NE	CW	NW	TP
SP	Mean	0.91	0.97	0.96	0.98	0.97	0.98
	Max	0.99	0.99	0.99	0.99	0.99	0.99
	Min	**0.64**	0.89	**0.60**	0.83	**0.73**	**0.78**
	Std	0.05	0.02	0.04	0.01	0.02	0.02
SU	Mean	0.92	0.96	0.96	0.97	0.99	0.97
	Max	0.98	0.99	0.99	0.99	0.99	0.99
	Min	0.84	**0.77**	0.85	0.86	0.97	0.86
	Std	0.03	0.03	0.02	0.03	0.00	0.03
FA	Mean	0.97	0.97	0.97	0.97	0.88	0.98
	Max	0.99	0.99	0.99	0.99	0.99	0.99
	Min	0.82	0.89	0.87	0.86	**0.64**	0.94
	Std	0.04	0.03	0.03	0.02	0.11	0.01
WI	Mean	0.92	0.92	0.89	0.95	0.92	0.97
	Max	0.99	0.99	0.99	0.99	0.99	0.99
	Min	**0.65**	**0.51**	**0.60**	**0.71**	**0.58**	**0.69**
	Std	0.07	0.07	0.09	0.04	0.07	0.03

Comment 5

How to define the rain-no-rain threshold?

Response:

As shown in figure below, the rain–no-rain threshold is set at about v_i (fig. b) where the cumulative frequency equals C_i (fig. a and b). Specially, all precipitation rate (Tb) are sorted in ascending (descending) order. Then cumulative probability distributions are both obtained. The cumulative probability is defined as critical probability when precipitation rate equals zero. The rain-no-rain threshold is the Tb with cumulative probability same as the critical probability. As shown in Fig. 2c and 2d (T means precipitation rate; V represents Tb), the rain–no-rain threshold is set at about vi where the cumulative probability equals Ci (critical probability). Please see line 11~15 in page 6 (red color).

Thanks again for your valuable advice.

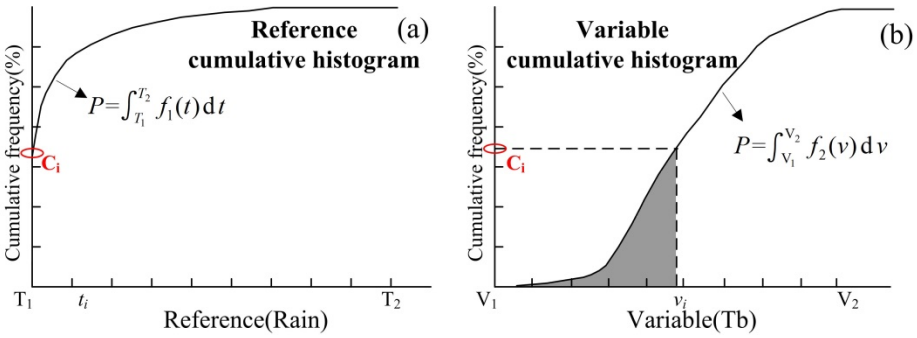

Comment 6

How the DCDF works for each region in each month, rather than seasonal? Figure 8 is for all regions?

Response:

It is unavailable for hourly gauge data. A disdrometer installed at Xingzi station (29.45°N, 116.05°E) in the Jiangxi province (Fig. 1) provided hourly data in 2014, except June and July when the instrument was subject to a transmission error. Figure 8 is just for a point using this disdrometer data at the hourly scale.

Table below lists the statistics (We only showed CC and Bias) at the daily scale for each region in each month. The results showed that DCDF generally performed at each month same as at each season.

Indexes	Month	Type	SE	CE	NE	CW	NW	TP
B(%)	Jan	CMORPH	-99.27	-34.28	-103.31	1294	205.31	1598
		DCDF	18.28	27.15	22.98	2159	185.94	1628
	Feb	CMORPH	-91.83	-33.94	-90.64	1323	67.24	1767
		DCDF	5.65	15.24	20.38	1642	39.29	2338
	Mar	CMORPH	-22.44	-3.92	-48.56	41.85	170.55	80.27
		DCDF	-10.61	2.72	40.90	50.72	197.69	96.51
	Apr	CMORPH	-20.45	-3.10	-43.72	45.86	153.91	82.25
		DCDF	-10.72	3.26	37.59	44.42	192.35	100.76
	May	CMORPH	-15.93	-3.10	-43.98	47.37	157.57	86.20
		DCDF	-6.61	2.95	30.26	55.19	187.38	104.40
	Jun	CMORPH	-16.83	2.29	5.61	-37.22	162.62	-20.68
		DCDF	-8.92	2.07	5.68	20.91	222.37	19.53

	Jul	CMORPH	-24.42	3.27	5.54	-46.77	153.39	-11.25
		DCDF	-15.57	2.98	5.80	25.62	218.35	16.17
	Aug	CMORPH	-25.25	3.00	7.02	-40.43	117.33	5.17
		DCDF	-14.90	2.63	7.16	29.85	197.94	10.36
	Sept	CMORPH	-68.59	-33.92	-17.58	19.90	120.25	41.33
		DCDF	9.39	30.28	16.68	15.47	118.37	54.45
	Oct	CMORPH	-69.99	-34.74	-19.21	9.18	118.69	45.95
		DCDF	11.57	36.56	12.70	17.37	130.66	58.72
	Nov	CMORPH	-50.36	-27.92	-12.15	11.29	112.30	48.99
		DCDF	0.21	39.88	20.33	9.86	116.71	62.28
	Dec	CMORPH	-95.41	-30.92	-91.95	921	61.25	1770
		DCDF	7.73	22.2	23.51	1623	50.22	1862
CC	Jan	CMORPH	0.30	0.01	0.00	0.06	0.03	0.05
		DCDF	0.45	0.16	0.04	0.01	0.02	0.11
	Feb	CMORPH	0.38	0.05	0.00	0.06	0.04	0.10
		DCDF	0.60	0.18	0.06	0.01	0.04	0.19
	Mar	CMORPH	0.57	0.31	0.36	0.20	0.07	0.00
		DCDF	0.63	0.39	0.35	0.16	0.06	0.01
	Apr	CMORPH	0.61	0.42	0.38	0.17	0.07	0.06
		DCDF	0.64	0.41	0.38	0.19	0.05	0.05
	May	CMORPH	0.67	0.34	0.36	0.17	0.07	0.09
		DCDF	0.71	0.45	0.38	0.17	0.05	0.08
	Jun	CMORPH	0.38	0.26	0.30	0.17	0.41	0.30
		DCDF	0.49	0.28	0.51	0.46	0.44	0.39
	Jul	CMORPH	0.36	0.17	0.24	0.17	0.40	0.22
		DCDF	0.47	0.27	0.44	0.44	0.45	0.35
	Aug	CMORPH	0.35	0.18	0.24	0.17	0.40	0.22
		DCDF	0.47	0.25	0.43	0.44	0.44	0.36
	Sept	CMORPH	0.39	0.48	0.36	0.07	0.31	0.19

	DCDF	0.54	0.50	0.44	0.09	0.20	0.08
Oct	CMORPH	0.41	0.48	0.36	0.07	0.32	0.10
	DCDF	0.51	0.52	0.50	0.09	0.20	0.08
Nov	CMORPH	0.42	0.54	0.36	0.07	0.35	0.06
	DCDF	0.52	0.54	0.51	0.14	0.26	0.08
Dec	CMORPH	0.33	0.02	0.00	0.05	0.02	0.06
	DCDF	0.47	0.16	0.06	0.00	0.02	0.17

Comment 7

Table 3, CDF => DCDF

Response:

Thank you for your useful advice. We have revised them. Please see table 2.

Comment 8

P7 L18: It seem => It seems

Response:

Thank you for your useful advice. We have revised them. Please see line 3 in page 10 (red color).

Comment 9

What is the specific means of a, b, c, and d in equations 11 to 13.

Response:

Thank you for your useful advice. These evaluation metrics in chapter 2.3 and 2.4 are well known, thus they have been deleted. We have removed chapter 2.3 and 2.4 also fig 3 (Schematic of the variogram curve), tab.1 (Contingency table for the definition of the categorical metrics).

Comment 10

Figure 7 is hard to follow. Please revise it in a more readable way.

Response:

Thank you for your useful advice. We have revised it. Please see fig. 5.

Comment 11

Some information is missing or wrong in Fig 9a.

Response:

Thank you for your useful advice. We have revised them. Please see line Fig 7a.

Precipitation downscaling using a probability-matching approach and geostationary infrared data: An evaluation over six climate regions

Ruifang Guo[1,2], Yuanbo Liu[1], Han Zhou[1,2], Yaqiao Zhu[3]

[1]Key Laboratory of Watershed Geographic Sciences, Nanjing Institute of Geography and Limnology, Chinese Academy of Sciences, No. 73 East Beijing Road, Nanjing 210008, China
[2]University of Chinese Academy of Sciences, No. 19 Yuquan Road, Beijing 100049, China
[3]College of Urban and Environmental Sciences, Hubei Normal University, No.11 Cihu road,Huangshi 435002, China

Correspondence to: Yuanbo Liu (ybliu@niglas.ac.cn)

Abstract. Precipitation is one of the most important components of the global water cycle. Precipitation data at high spatial and temporal resolutions are crucial for basin-scale hydrological and meteorological studies. In this study, we propose a cumulative distribution of frequency (CDF)-based downscaling method (DCDF) to obtain hourly 0.05°×0.05° precipitation data. The main hypothesis is that a variable with the same resolution of target data should produce a CDF that is similar to the reference data. The method was demonstrated using the 3 hourly 0.25°×0.25° Climate Prediction Center Morphing method (CMORPH) dataset and the hourly 0.05°×0.05° FY2-E Geostationary (GEO) Infrared (IR) temperature brightness (Tb) data. Initially, power function relationships were established between precipitation rate and Tb for each 1°×1° region. Then the CMORPH data were downscaled to 0.05°×0.05°. The downscaled results were validated over diverse rainfall regimes in China. Within each rainfall regime, the fitting functions coefficients were able to implicitly reflect the characteristics of precipitation. Quantitatively, the downscaled estimates not only improved spatio-temporal resolutions, but also performed better (Bias: -7.35%~10.35%; correlation coefficient (CC): 0.48~0.60) than the CMORPH product (Bias: 20.82%~94.19%; CC: 0.31~0.59) over convective precipitating regions. The downscaled results performed as well as the CMORPH product over regions dominated with frontal rain systems and performed relatively poorly over mountainous or hilly areas where orographic rain systems dominate. Qualitatively, at the daily scale, DCDF and CMORPH had nearly equivalent performances at the regional scale, and 79% DCDF may perform better than or nearly equivalent to CMORPH at the point (rain gauge) scale. The downscaled estimates were able to capture more details about rainfall motions and changes under the condition that DCDF perform better than or nearly equivalent to CMORPH.

1 Introduction

Precipitation is a critical component in the global water cycle (Barrett and Martin, 1981; Smith et al., 1998; Tobler, 2004). Precipitation data at spatio-temporal resolutions are favoured mainly for two reasons. First, the poor representativeness and unevenly distribution of gauge stations make it incapable of reflecting spatially the precipitation variations (Hughes, 2006, Collischonn et al., 2008; Javanmard et al., 2010). Second, ground radar systems can provide full coverage spatial data for

most regions, but RADAR is very week in view of the precipitation intensity and subject to short time series. Moreover, the validation poses a big challenge for hydrological applications (Krajewski and Smith, 2002).

A number of techniques have been developed to estimate or retrieve precipitation (Kidd and Levizzani, 2011). Based on these technologies, precipitation datasets have been produced at various resolutions, including the Global Precipitation Climatology Project (GPCP) (Huffman et al., 1997, 2001, 2009), the Tropical Rainfall Measuring Mission (TRMM) Multi-Satellite Precipitation (TMPA) (Huffman et al., 2007), the Climate Prediction Center Morphing method (CMORPH) (Joyce et al., 2004) and the Global Satellite Mapping of Precipitation (GSMaP) (Ushio et al., 2009), especially over the last 20 years. The typical spatial resolution of these products is 0.25°×0.25° (Dinku et al., 2007; Ebert et al., 2007; Hirpa et al., 2010; Sohn et al., 2010; Bitew and Gebremichael, 2011; Romilly and Gebremichael, 2011; Thiemig et al., 2012; Hu et al., 2014). This coarse resolution generally impedes the applications of the data for basin-scale hydrological and meteorological studies (Mekonnen et al., 2008). A downscaling procedure would therefore be highly necessary to meet the requirements of small-scale (<10 km) applications.

Downscaling approaches was first used to interpolate regional-scale atmospheric predictor variables to point-scale meteorological series (Karl et al., 1990; Wigley et al., 1990; Hay et al., 1991; 1992). Currently, downscaling approach is well developed and can be categorized into regression method, weather pattern approach, stochastic weather generator and limited-area climate modelling (Wilby and Wigley, 1997; Cannon, 2008). Most methods are based on meteorological or climate models, and assume that relationships can be established between atmospheric parameters at disparate temporal and/or spatial scales (Giorgi and Mearns, 1999; Willems and Vrac, 2011; Kenabatho et al., 2012). In another way, downscaling approach is categorized into dynamical method (using regional climate models to translate the large-scale weather evolution into a physically consistent evolution at higher resolution) and statistical method (based on statistical relationships between the regional climate and large-scale predictor variables) (Schmidli et al., 2006). At present, these methods are generally available to downscale general circulation models (GCMs) data.

Various downscaling techniques have been developed to improve the resolution of satellite precipitation data. Immerzeel et al. (2009) used an exponential relationship between 1-km Normalized Difference Vegetation Index (NDVI) and precipitation to downscale TRMM 3B43 precipitation data on the Iberian Peninsula. Jia et al. (2011) used a linear regression relationship between a combination of NDVI/DEM and precipitation to downscale TRMM 3B43 precipitation data in the Qaidam Basin of China. Duan and Bastiaanssen (2013) used a two-degree polynomial regression model between NDVI and precipitation to downscale TRMM 3B43 precipitation data in the Lake Tana Basin, Ethiopia and the Caspian Sea Region, Iran. These studies manifest the potential of downscaling methods to obtain fine-resolution precipitation (<10km), while mainly focus on precipitation data with low temporal resolutions (i.e., annual or monthly).

The main objective of this study is to develop a regression-based downscaling method to obtain precipitation estimates with a high spatio-temporal resolution (0.05°, hourly). Barrett et al. (1991) proposed a cumulative histogram method to relate precipitation observations to satellite estimates in an effort to avoid bias problems related to simple regression. In this study, we propose a cumulative distribution of frequency (CDF)-based downscaling method (DCDF) and perform a preliminary

validation using CMORPH and geostationary (GEO) infrared (IR) temperature brightness (Tb) data. This new method can 1) lead to a better understanding of satellite precipitation data and 2) stimulate scientific interests to engender the development of precipitation data with improved resolutions. The following section introduces the principle, framework and procedure of the downscaling method. Section 3 details the test areas and data processing. Section 4 presents the major findings followed by discussion in section 5. Finally, section 6 concludes.

2 Study areas and datasets

2.1 Study areas

Existing studies confirmed that the performances of satellite precipitation estimates are highly dependent on the rainfall regime (Arkin et al., 2006; Ebert et al., 2007; Gottschalck et al., 2005), which varies with climate zone, latitude, longitude and elevation. Thus, six 5°× 5° regions were selected for validation (Fig. 1). Their corresponding geographic and climatic characteristics are listed in Table 1. These areas are distributed from south to north and from east to west, and they incorporate most rainfall regimes.

Among the six regions, regions SE, CE and NE are located in the eastern monsoon region. It is warm and rainy during the southeast monsoon in June-August, and cold and dry during the northwest monsoon in December-February. These three regions are featured by low-elevation hills and plains. Regions CW, NW and TP are located in the non-monsoon region with a continental climate. CW and NW belong to arid region, with 60%~70% precipitation occurring in June-August. CW has a relatively high elevation, mainly covered by plateaus, mountains and basins. NW is mainly covered by plateaus and basins. TP has a complex climate, mainly covered by plateaus and mountains. The seasonal precipitation distribution has two forms: a unimodal distribution in summer (June-August), and a bimodal distribution in spring (March-May) and autumn (September-November).

2.2 Datasets

2.2.1 Meteorological data

Rain gauge data were obtained from the National Meteorological Information Centre of the China Meteorological Administration (CMA) (http://cdc.cma.gov.cn/home.do). The datasets include daily precipitation records at 137 rain gauge stations in 2014 (Fig. 1). A strict quality control has been applied to check extreme values (Ma, 1998). There are 33, 29, 14, 31, 12 and 18 rain gauges in regions SE, CE, NE, CW, NW and TP, respectively. In the case of more than one station located within a pixel, the rain gauge values are averaged to represent the grid value. Statistical analyses were used to evaluate precipitation estimates at the daily scale. In addition, a disdrometer installed at Xingzi station (29.45°N, 116.05°E) in the Jiangxi province (Fig. 1) provided hourly data in 2014, except June and July when the instrument was subject to a transmission error. Disdrometer data is used to evaluate the precipitation estimates.

2.2.2 Satellite data

IR data (10.7 μm) were collected from the Stretched Visible and Infrared Spin Scan Radiometer (S-VISSR) onboard FY2-E satellite. The data are available at National Satellite Meteorology Center (http://satellite.nsmc.org.cn/). FY2-E provides hourly coverage of eastern Asia from 75°S to 75°N. The IR Tb data were corrected for zenith angle viewing effects.

CMORPH is developed and produced by the Climate Prediction Center (CPC) in the National Oceanic and Atmospheric Administration (NOAA). CMORPH produces 0.25°×0.25° 3 hourly global precipitation data using PMW and IR data. PMW data are from Microwave Imager (TMI) on TRMM, Special Sensor Microwave Imager (SSM/I) on Defense Meteorological Satellite Program (DMSP) satellites 13-15, Advanced Microwave Scanning Radiometer-Earth Observing System (AMSR-E) on Aqua, and Advanced Microwave Sounding Unit-B (AMSU-B) on NOAA satellite 15-18. Precipitation estimates are generated with the algorithms of Ferraro (1997) for SSM/I, Ferraro et al. (2000) for AMSU-B and Kummerow et al. (2001) for TMI. IR data are obtained from the GEO Operational Environmental Satellites (GOES) 8/10, European Meteorological Satellites (Meteosat) 5/7 and Japanese GEO Meteorological Satellites (GMS) 5. CMORPH uses motion vectors derived from GEO satellite IR imagery to propagate the relatively high quality precipitation estimates derived from PMW data (Joyce et al., 2004). Hence, quantitative precipitation estimates are based solely on PMW data. GEO-IR data are not used to estimate precipitation but rather to interpolate between two PMW-derived precipitation rate fields.

3 Methodology

3.1 CDF matching

The CDF matching is a probability based process. It assumes a variable (v) should produce a similar CDF to the reference variable (t). The frequencies of t and v are shown in Equations (1)-(2), and the cumulative frequencies in Eqs. (3)-(4).

$$P_t = f_1(t) \tag{1}$$

$$P_v = f_2(v) \tag{2}$$

$$C_t(t) = \int_{T_1}^{t} f_1(t)\,\mathrm{d}t \tag{3}$$

$$C_v(v) = \int_{V_1}^{v} f_2(v)\,\mathrm{d}v \tag{4}$$

$$C_v^{-1}[C_t(t)] \xrightarrow{f_3} t \tag{5}$$

where P_t and P_v are the probability of t and v, $f_1(t)$ and $f_2(v)$ are probability density functions of t and v, and $C_t(t)$ and $C_v(v)$ are the cumulative density functions of t and v, respectively. $f_3(v)$ represents relationship between t and v.

The steps for CDF matching are summarized in Fig. 2. First, t and v are shown into histograms (Fig. 2a and Fig. 2b). The frequency of an arbitrary point t_i (or v_i) on the $f_1(t)$ [or $f_2(v)$] curve can be expressed as $P(t=t_i)=f_1(t_i)$ [or $P(v=v_i)=f_2(v_i)$].

Second, these histograms are transformed into cumulative histograms (Fig. 2c and Fig. 2d). The cumulative frequency of an arbitrary point t_i (or v_i) on the $C_t(t)$ [or $C_v(v)$] curve can be expressed as $C(t < t_i) = \int_{T_1}^{t_i} f_1(t)dt$ [or $C(v < v_i) = \int_{V_1}^{v_i} f_2(v)dv$].

Third, these cumulative histograms are matched so that *v* has a cumulative histogram similar to *t*. The matching process is implemented by a one-to-one mapping CDF of variable onto that of the reference (Eq. 5). Last, the *v*-to-*t* relationship is established (Eq. 5) (Fig. 2e). Magnusson et al. (2015) demonstrated that CDF matching works better than histogram-matching method when low values have high frequencies, which is generally the case for precipitation.

3.2 Downscaling

Our method is based on the work of Barrett et al. (1991) and Kidd and Levizzani (2011). Rainfall can be inferred from IR imagery because heavy rainfall tends to be associated with large, tall clouds with cold cloud tops. Therefore, empirical relationships between precipitation rate and Tb are derived (Arkin and Meisner, 1987; Greene and Morrissey, 2000; Prigent, 2010). However, these relationships are indirect, and exhibit significant variations during the lifetime of a rainfall event. They also differ among rain systems and climatological regimes, which cause large uncertainties in precipitation estimations (Kidd and Levizzani, 2011). Ba and Gruce (2001) demonstrated that a two-degree polynomial model is more effective for describing the relationship, and that the coefficients of the model are regional dependent. Overall, the precipitation-Tb relationship is highly variable over time and space.

Microwave (MW) radiation reflects the physical structures of clouds. Emission from rain droplets increase MW radiation, and scattering by precipitating ice particles decreases MW radiation. Although MW techniques are physically more direct than those based on IR radiation, they both can reflect rainfall events. Therefore, we assume that IR signal produces a similar frequency distribution of precipitation rates to MW signal over a certain region during a certain period. Barrett et al. (1991) proposed a cumulative-histogram-matching method to relate rainfall observations to satellite precipitation data. Kidd et al. (2003) applied the same method to estimate rainfall using passive microwave (PMW) and IR data over Africa.

The assumptions behind the downscaling method include 1) Tb has similar cumulative frequency as precipitation rate at certain spatial and temporal scales, and 2) satellite precipitation products provide relatively accurate estimates with low spatial and temporal resolutions. In contrast, GEO-IR data have high spatio-temporal resolution yet with low accuracy. Illustrated in Fig. 3, the downscaling method explores the advantages of satellite precipitation product and GEO-IR data. Specifically, 1) to aggregate Tb (Tb_h) from a high resolution to a low resolution (Tb_l) similar to the precipitation data (Eq. 6), and 2) to apply the CDF matching to the Tb_l and precipitation rate (R_l) to obtain a Tb_l-R_l relationship and a rain-no-rain threshold (Eq. 7). The downscaled precipitation rates are estimated based on the Tb_l-R_l relationships (Eq. 8).

$$Tb_l = \frac{1}{n}\sum_{i=0}^{n} Tb_h(i) \tag{6}$$

$$Tb_l = m \times R_l^e \tag{7}$$

$$R_h = \left(\frac{Tb_h}{m}\right)^{1/e} \tag{8}$$

where Tb_h denotes high-resolution GEO-IR Tb data. Tb_l denotes upscaled Tb data. R_l denotes the low-resolution precipitation product. R_h denotes the derived high-resolution estimates. m and e are coefficients of the Tb-R relationship, and n is the number of high-resolution pixels within a low-resolution pixel.

Under the assumption that colder clouds are linked to higher rainfall than warmer clouds, the downscaling method assumes a monotonically increasing precipitation rate with decreasing Tb. Therefore, cumulative histograms of precipitation rate and Tb are matched, so that the occurrence of the heaviest precipitation is associated with the Tb values linked to the heaviest rainfall. Decreasing Tb values are assigned to increasing precipitation rates so that the final distribution of Tb assigned to the precipitation rates is the same as that determined using precipitation rate data. Specially, all precipitation rate (Tb) are sorted in ascending (descending) order. Then cumulative probability distributions are both obtained. The cumulative probability is defined as critical probability when precipitation rate equals zero. The rain-no-rain threshold is the Tb with cumulative probability same as the critical probability. As shown in Fig. 2c and 2d (T means precipitation rate; V represents Tb), the rain–no-rain threshold is set at about v_i where the cumulative probability equals C_i (critical probability).

The specific steps used for downscaling with CMORPH and FY2-E IR data are described as follows:

a. Aggregate IR-Tb data ($Tb_{0.05}$) from 0.05° to 0.25° by pixel averaging ($Tb_{0.25}$).

IR-Tb data ($Tb_{0.05}$) were aggregated to a 0.25° grid ($Tb_{0.25}$) for each 3-hour period (0000-0300, 0300-0600, . . ., 2100-2400 UTC), in order to match the spatial and temporal resolutions as CMORPH.

b. Generate the histogram database for CDF matching.

IR-Tb ($Tb_{0.25}$) and CMORPH precipitation rate ($R_{0.25}$) were recorded in a database. The sample area for CDF matching was determined as follows. The horizontal and temporal scales of stratiform precipitation range from 10^1 to 10^3 kilometers and from hours to days (Orlanski, 1975; Trapp, 2013), while those of cumuliform precipitation range from a few km to tens of kilometers and from minutes to hours (Orlanski, 1975; Rickenbach, 2008). In combination with previous studies (Kidd et al., 2003; Huffman et al. 2007), the downscaling procedure was conducted at 1°×1° grids over a 10-days period. To reduce the heterogeneity among grids, a 3×3 window was used for smoothing purpose.

c. Build relationships between precipitation rate and Tb

The histograms of Tb and precipitation rate were generated and converted to cumulative histograms, and then matched using the CDF matching (As shown in fig. 2. precipitation rate means T; Tb represents V; v_i is the rain-no-rain threshold). Power function relationship between precipitation rate ($R_{0.25}$) and Tb ($Tb_{0.25}$) was established for each 1°×1° area over a 10-days period. Meanwhile, various parameters, including coefficients of the Tb-R relationship, rain-no-rain threshold and R^2, were obtained.

d. Estimate precipitation rate pixel by pixel at 1-hour, 0.05°

All pixels in the Tb images ($Tb_{0.05}$) were divided into two categories, raining ones less than the rain-no-rain threshold and non-raining ones larger than the threshold. Tb-R relationships were applied to these raining pixels. Finally, CMORPH data were downscaled to 1-hour, 0.05°×0.05°.

3.3 Variogram

A variogram describes how data correlates with distance. The variogram function γ(h) is defined as half of the mean value of the square of the difference between points separated by a distance h (Matheron, 1963). A variogram is generally an increasing function of distance h. The relationship between γ(h) and h is commonly described using the nugget effect (C_0), sill (C_0+C) and range (D). C_0 denotes micro-scale variations, equated to of γ(0). C_0+C denotes limit of the variogram γ (+∞). D denotes the distance at which the difference of the variogram from the sill becomes negligible. Variogram is used here to describe the spatial structure of satellite precipitation data.

4 Results

4.1 Tb-precipitation rate relationship

Fig. 4 shows fitting functions between the precipitation rate and Tb within each 1°×1° grid. It was observed that Tb had a power function relationship with the precipitation rate. With an increase in the precipitation rate, Tb decreased, and the rate of change also reduced. The model fitting R^2 were all higher than 0.90. From the region SE to NE, the precipitation rate decreases, mainly subject to latitude. The maximum precipitation rate, rain-no-rain threshold and R^2 all showed decreasing trends. The maximum precipitation rate was 19.9 mm/h in region SE, 9.8 mm/h in region CE and 4.3 mm/h in region NE. The corresponding Tb values were 198 K, 202 K and 210 K, respectively, and the rain-no-rain threshold values were 265 K, 259 K and 249 K. The probability of precipitation rate was the largest for a given Tb in region SE, followed by region CE and then region NE. Regions CW and NW are arid, while TP is humid. The maximum precipitation rate was 3.5 mm/h for both region CW and NW and 11 mm/h for region TP. The rain-no-rain thresholds for regions CW and NW were approximately 230 K, while 254K for region TP. The probability of precipitation rate was the largest for a given Tb in region TP, because region TP has a complex rain system and high elevation. Generally, the fitting relationships reflected precipitation characteristics well.

4.2 Estimation results

Fig. 5 shows a comparison of the spatial distributions of CMORPH and DCDF precipitation estimates regions SE, NE and TP. The downscaled precipitation showed a similar spatial distribution to CMORPH, yet it reflected more detailed moving and changing processes of rainfall. To demonstrate clouds captured through DCDF and CMORPH, region SE was exemplified (14:00 to 16:00 June 21, 2014). Three cloud centers were observed in the southeastern and mid-eastern parts at

14:00. One hour later, two centers in the southeast moved eastward and joined together, while another center moved eastward. Two precipitation centers continued to move eastward at 16:00. In addition, D and sill values of DCDF (2.796 and 1.070) were higher than those of CMORPH (1.614 and 0.489). Large range and sill values indicate a high spatial dependence and high spatial variability. Thus, the spatial dependence and variability for high-resolution data were generally larger those for low-resolution data.

In region SE, clouds were relatively centralized with a high precipitation rate and were small in size. In region NE, clouds were discrete with a low precipitation rate and were widely distributed. In region TP, both centralized and discrete clouds appeared. Cumuliform cloud is the main type in region SE, while stratiform cloud is dominant in region NE, and both in region TP. Thus, the cloud distributions obtained through satellite data, especially using the DCDF approach, were consistent with the local characteristics. Sill for cumuliform clouds was larger than that for stratiform clouds. A larger sill value was obtained for region SE (DCDF: 1.070; CMORPH: 0.489) than for region NE (DCDF: 0.007; CMORPH: 0.008). These results indicated that the DCDF method can reflect precipitation characteristics among rain systems and climatological regimes.

4.3 Validation

Fig. 6 shows a comparison among the DCDF, CMORPH and disdrometer at the hourly scale. The DCDF and CMORPH were able to capture rainfall events, although they differed in magnitude from the reference data in some cases. The DCDF effectively reflected the peak of each rainfall event, but could not exactly identify same starting and ending times of rainy events, resulting in somewhat delayed or advanced rainfall. The DCDF may detect non-rainy events as rainy events especially in dry seasons. CMORPH reported low-rain events as non-rainy events. Both of the DCDF and CMORPH estimates coincided with disdrometer data at precipitation rates ranging from 1 to 10 $mm \cdot h^{-1}$, such as the events from 10:00 to 14:00 on February 9 and from 21:00 on May 13th to 10:00 on May 14th.

To demonstrate performance of the DCDF method, a comparison of the DCDF and CMORPH estimates was conducted at the regional scale and at the point (rain gauge) scale. Fig. 7 shows the average precipitation of each region derived from rain gauge, DCDF and CMORPH. The daily average precipitation over each region showed almost identical temporal variations for DCDF and CMORPH. Both DCDF and CMORPH showed similar temporal patterns to the rain gauge observations, but they were probably subject to underestimation for regions CW and NW and overestimation for regions SE and TP. At the point (gauge) scale, the better fit between DCDF and gauge data than that between CMORPH and gauge data is 10%. The nearly equivalent fit is 69%. The poorer fit mainly happened in region NW, CW and TP. Fig. 8 shows cases of better fit that the time series of DCDF were generally more consistent with the rain gauge data than CMORPH, although the DCDF series were occasionally deviated from gauge data or misreported non-rainy events as rainy events. These results indicated that both DCDF and CMORPH demonstrated nearly equivalent performances at the regional scale, and 79% DCDF may perform better than or nearly equivalent to CMORPH at the point (gauge) scale.

Table 2 lists the seasonal statistics for the six regions at the daily scale. Generally, DCDF performed better than CMORPH in region SE, while performed equivalently to CMORPH in regions CE and NE. Both of the DCDF and CMORPH showed better performances during rainy season. The DCDF generally showed the smallest biases between -7.35% and 10.35% (CC: 0.48~0.60) in region SE, and overestimated precipitation by 2.66%-33.95% (CC: 0.05~0.53) in regions CE and NE. CMORPH underestimated precipitation by 20.82%-94.19% (CC: 0.31~0.59) in region SE and showed biases between -93.2% and 6.78% (CC: 0.00~0.50) in regions CE and NE. Both the DCDF and CMORPH both exhibited bad performances in regions CW, NW and TP, and showed large biases (-73.75~2106%), low CC values (0.01~0.44) and high FAR values (0.33~1.00) during the winter. Further inspection showed that the DCDF overestimation was due to high POD and FAR, which may be caused by a low rain-no-rain threshold. The large biases for regions CW, NW and TP were likely due to insensitivity of precipitation data to very low precipitation in arid regions, and inability to estimate precipitation over mountainous or hilly areas where orographic rain systems dominate.

5 Discussion

Existing downscaling methods involved an assumption that local scale patterns are driven by large-scale climatic fluctuations (Wilby and Wigley, 1997; Wilby et al., 2002). Most of these methods rely on meteorological or climate models, and utilize multiple parameters, such as temperature, humidity, pressure, vorticity and geostrophic airflow. These methods are not used to downscale satellite precipitation products possibly due to a diversity of parameters and complexity of the meteorological and climate models. In contrast, the DCDF method in this study assumes that IR retrieval should produce a frequency distribution of precipitation rates similar to that produced by of MW retrievals over a certain region during a certain period. That is, IR estimations and MW retrievals from clouds have strong statistical frequency similarities.

Due to high spatial and temporal variability of precipitation, the DCDF method must be conducted over a certain region during a certain period. The area and time period must be large enough for a reasonable sample size, but small enough to represent local characteristics. In the TMPA algorithm, relationship between IR and precipitation rate is built within a 1°×1° area by 3×3 windows over the period of a month (Huffman et al. 2007). Kidd et al. (2003) obtained the relationship within 1°×1° area with the use of a 5°×5° Gaussian filter over a period of 5 days. Based on the horizontal and temporal scales of stratiform and cumuliform precipitation (Orlanski, 1975; Rickenbach, 2008, Trapp, 2013) and previous studies (Kidd et al., 2003; Huffman et al. 2007), the DCDF method is applied within a 1°×1° area by 3×3 windows over a 10-day period. Nevertheless, the same gridded sample area is not the optimal selection. The size of sample area is determined according to local cloud type, and varies over space and time. It likely is our future work to improve precipitation estimates algorithm.

It seems that IR data are used twice, one for original CMORPH generation and the other for downscaling CMORPH. In fact, IR data serve as an intermediate variable for an interpolation purpose in the first step. While IR data serve as an ancillary variable in the second step for developing a precipitation-Tb relationship. The CMORPH product is essentially derived from MV observations, and therefore the use of IR data is reasonable. We selected CMORPH as reference

precipitation data mainly for following reasons. Products with similar resolutions to GEO-IR data (0.05°) are not used, such as CMORPH at 0.072° and GSMaP at 0.1°. TRMM 3B42 (RT) and Naval Research Laboratory Blended (NRLB) (Turk, 2005) algorithm combine MW-calibrated IR estimates, which would result in IR reusage.

The DCDF method has two main disadvantages. The physical premise of the DCDF method is that cloud top temperature in the IR imagery is a simple empirical function of cloud top height, and that heavier rainfall tends to be associated with larger, taller clouds with colder cloud tops. Unfortunately, not all cold clouds precipitate, and precipitation does not always fall from cold clouds only (Barrett, 1970). This phenomenon results in misreporting. In addition, the rain-no-rain threshold is very critical for final precipitation estimates. The size of the sample area and the indirect relationship between IR-Tb and precipitation rate both affect the rain-no-rain threshold. However, both of them have uncertainties among rain systems and climatological regimes, resulting in uncertainties of rain-no-rain threshold.

Rain-gauge measure represents a space for a very small area while satellite precipitation products have a spatial resolution of several kilometers or more. Thus, high-resolution data is generally more similar to gauge data than low-resolution data. Furthermore, the characteristic scale is small for convective systems, and large for frontal rain systems. Convective precipitation dominates in region SE, while frontal rain system dominates in regions CE and NE. Thus, a rain gauge measure can represent a space for a smaller area in region SE than in regions CE and NE. Therefore, discrepancies between rain gauge observations and satellite estimates are lower in region SE than in regions CE and NE. CMORPH performed poorly in regions NW and TP, where orographic rain systems dominate (Hirpa et al., 2010; Romilly and Gebremichael, 2011; Gao and Liu, 2013). Our results are consistent with these findings.

It is expected that the DCDF method also applied to reanalysis precipitation data (e.g. ERA-Interim, 0.75°/6 hourly). First, the assumption that Tb has similar cumulative frequency as precipitation rate at certain spatial and temporal scales is also applied to reanalysis data. Second, the most average of R^2 between Tb and CMORPH are higher than 0.90, which may infer that the bad performance of the DCDF approach in winter and in mountainous regions is mainly caused by low accuracy of CMORPH. Thus using reanalysis data for downscaling may be better than satellite products.

6 Conclusions

Precipitation data with high spatial and temporal resolutions are highly needed in basin-scale hydrological and meteorological studies. Based on the works by Barrett et al. (1991) and Kidd and Levizzani (2011), this study proposed a DCDF method to obtain precipitation data at the hourly, 0.05° scale. The method was demonstrated using the CMORPH dataset and FY2-E GEO-IR Tb data in 2014. With the establishment of a power function relationship, improved precipitation estimates at the hourly and 0.05° resolution were produced. The DCDF precipitation estimates were validated using rain gauge data at six 5°× 5° regions with different climate and geographical conditions in China.

There are three key points of the DCDF method. First, it explores the advantages of satellite precipitation estimates and GEO-IR data. The DCDF method assumes a monotonically decreasing Tb rate with an increase of precipitation rate, and that

Tb data have the same cumulative frequency as that of precipitation rate for certain spatial and temporal scales. The matching process is implemented by quantile-mapping the CDF of Tb onto that of precipitation rate. Second, the sample area where the CDF matching was conducted needs to be large enough for a reasonable sample size, but small enough to represent the local characteristics. In this study, size of the sample area was 1° × 1° grid over a 10-day period based on the characteristic scale of precipitation clouds. Third, a power function relationship between precipitation rate and Tb was established for each sample area. Meanwhile, a rain-no-rain threshold was obtained as the Tb value with the same cumulative frequency as that of precipitation rate defined at the critical point of rain-no-rain. Generally, the threshold was the maximum Tb in the CDF matching procedure.

The established fitting relationships generally reflected the precipitation characteristics well in the six validation regions. For the distributions of precipitation clouds, the DCDF precipitation estimates showed a similar spatial distribution to that produced by CMORPH, but it reflected more detailed moving and changing processes of rainfall under the condition that DCDF performed better than or nearly equivalent to CMORPH. The DCDF method can effectively reflect the precipitation characteristics among rain systems and climatological regimes. At the hourly scale, both DCDF and CMORPH coincided with the disdrometer data at precipitation rates ranging from 1 to 10 $mm \cdot h^{-1}$. The DCDF effectively reflected the peak of each rainfall event, but could not exactly identify the starting and ending times of rainy events. The DCDF may detect non-rainy events as rainy events especially in dry seasons, while CMORPH reported low-rain events as non-rainy events. At the daily scale, DCDF and CMORPH had nearly equivalent performances at the regional scale, and 79% DCDF may perform better than or nearly equivalent to CMORPH at the point (rain gauge) scale. Generally, the DCDF performed better (bias: 7.35%~10.35%; CC: 0.48~0.60) than the original CMORPH product (bias: 20.82%-94.19%; CC: 0.31~0.59) over the regions where convective precipitation dominates. It performed as well as the CMORPH product over the regions where frontal rain systems dominate, and relatively poorly over mountainous or hilly areas, where orographic rain systems dominate.

Competing interests. The authors declare that they have no conflict of interest.

Acknowledgments and data

This work was partially supported by the State Key Program of the National Natural Science of China under Grant 41430855 and by the National High Technology Research and Development Program under Grant 2013AA12A301. The authors would like to thank Prof. Kidd (Dr Chris Kidd) for providing a report of SSM/I rainfall algorithms, and Prof. Xie (Dr Pingping Xie) for his guidance at the University of Maryland. The authors would like to thank research associate Bo Zhong and Mr Shanlong Wu for data collection and processing at the Institute of Remote Sensing and Digital Earth (RADI), Chinese

Academy of Sciences. The data used to produce the results of this paper may be obtained by contacting the corresponding author.

References

Arkin, P. A. and Meisner, B. N.: The relationship between large-scale convective rainfall and cold cloud over the western hemisphere during 1982-84, Mon. Weather Rev., 115(115), 51, doi: 10.1175/1520-0493(1987)115<0051:TRBLSC>2.0.CO;2, 1987.

Arkin, P., Turk, J., Ebert, B., Bauer, P., and Sapiano, M.: Evaluation of high resolution precipitation forecasts and analyses from satellite observations, in: AGU Fall Meeting, American Geophysical Union, 1: 4, 2006

Ba, M. B. and Gruber, A.: GOES multispectral rainfall algorithm (GMSRA), J. Appl. Meteorol., 40, 1500-1514, doi: 10.1175/1520-0450(2001)040<1500:GMRAG>2.0.CO;2, 2001.

Barrett E, C.: The Estimation of Monthly Rainfall from Satellite Data, Mon. Weather Rev., 98(4), doi: 10.1175/1520-0493(1970)098<0322:TEOMRF>2.3.CO;2, 1970

Barrett, E. C. and Martin, D. W.: The Use of Satellite Data in Rainfall Monitoring, Academic Press, London, 1981.

Barrett, E. C., Beaumont, M. J., Brown, K. A., and Kidd, C.: Development and testing of SSM/I rainfall algorithms for regional and global use: NA86AA-H-RA001, Final Rep. to the U.S. Dept. of Commerce, Washington, DC, 77, 1991.

Bitew, M. M. and Gebremichael, M.: Assessment of satellite rainfall products for streamflow simulation in medium watersheds of the ethiopian highlands, Hydrol. Earth Syst. Sci., 15(4), 1147-1155, doi: 10.5194/hess-15-1147-2011, 2011.

Cannon, A. J.: Probabilistic Multisite Precipitation Downscaling by an Expanded Bernoulli–Gamma Density Network, J. Hydrometeor., 9(6):1284-1300, doi: 10.1175/2008JHM960.1, 2008.

Chen, S., Hong, Y., Cao, Q., Gourley, J. J., Kirstetter, P. E., Yong, B., Tian, Y., Zhang, Z., Shen, Y., Hu, J., and Hardy, J.: Similarity and difference of the two successive v6 and v7 trmm multisatellite precipitation analysis performance over china, J. Geophys. Res. Atmos., 118(23), 13060-13074, doi: 10.1002/2013JD019964, 2013

Collischonn, B., Collischonn, W., Carlos, E., and Morelli, T.: Daily hydrological modeling in the Amazon basin using TRMM rainfall estimates, J. Hydrol, 360, 207-216, doi: 10.1016/j.jhydrol.2008.07.032, 2008.

Dinku, T., Ceccato, P., Lemma, M., Connor, S. J., and Ropelewski, C. F.: Validation of satellite rainfall products over east africa's complex topography, Int. J. Remote Sens, 28(7), 1503-1526, doi: org/10.1080/01431160600954688, 2007.

Duan, Z. and Bastiaanssen, W. G. M.: First results from Version 7 TRMM 3B43 precipitation product in combination with a new downscaling-calibration procedure, Remote Sens. Environ., 131, 1-13, doi: org/10.1016/j.rse.2012.12.002, 2013.

Ebert, E.E., Janowiak, J.E., and Kidd, C.: Comparison of near real time precipitation estimates from satellite observations and numerical models, Bull. Amer. Meteor. Soc., 88, 47-64, doi: 10.1175/BAMS-88-1-47, 2007.

Ferraro, R. R., Weng, F., Grody, N. C., and Zhao, L.: Precipitation characteristics over land from the noaa-15 amsu sensor, Geophys. Res. Lett., 27(17), 2669–2672, doi: 10.1029/2000GL011665, 2000.

Ferraro, R. R.: Special sensor microwave imager derived global rainfall estimates for climatological applications, J. Geophys. Res., 102(1021), 16715-16736, doi: 10.1029/97JD01210, 1997.

Gao, Y. C. and Liu, M. F.: Evaluation of high-resolution satellite precipitation products using rain gauge observations over the Tibetan Plateau, Hydrol. Earth Syst. Sci, 17, 837-849, doi: 10.5194/hess-17-837-2013, 2013.

Giorgi, F. and Mearns, L. O.: Introduction to special section: regional climate modeling revisited, J. Geophys. Res., 104, 6335–6352, doi: 10.1029/98JD02072, 1999.

Gottschalck, J., Meng, J., Rodell, M., and Houser, P.: Analysis of multiple precipitation products and preliminary assessment of their impact on global land data assimilation system land surface states, J. Hydrometeor., 6(5), 573-598, doi: 10.1175/JHM437.1, 2005.

Greene, J. S. and Morrissey, M. L.: Validation and uncertainty analysis of satellite rainfall algorithms, Prof. Geogr., 52(2), 247–258, doi: org/10.1111/j.0033-0124.2000.t01-1-.x, 2000.

Hay, L. E., Mccabe, G. J., Wolock, D. M., and Ayers, M. A.: Simulation of precipitation by weather type analysis, Water Resour. Res., 27(4), 493-501, doi: 10.1029/90WR02650, 1991.

Hirpa, F. A., Gebremichael, M., and Hopson, T.: Evaluation of High-Resolution Satellite Precipitation Products over Very Complex Terrain in Ethiopia, J. Appl. Meteorol. Clim., 49(5), 1044-4051, doi: 10.1175/2009JAMC2298.1, 2009.

Hu, Q., Yang, D., Li, Z., Mishra, A. K., Wang, Y., and Yang, H.: Multi-scale evaluation of six high-resolution satellite monthly rainfall estimates over a humid region in china with dense rain gauges. Int. J. Remote Sens, 35(4), 1272-1294, doi: org/10.1080/01431161.2013.876118, 2014.

Huffman, G. J., Adler, R. F., Arkin, P. A., Chang, A., Ferraro, R., Gruber, A., Janowiak, J., Mcnab, A., Rudolf, B., and Schneider, U.: The Global Precipitation Climatology Project (GPCP) combined precipitation data set, Bull. Amer. Meteor. Soc., 78, 5-20, doi: 10.1175/1520-0477(1997)078<0005:TGPCPG>2.0.CO;2, 1997.

Huffman, G. J., Adler, R. F., Bolvin, D. T., and Gu, G.: Improving the global precipitation record: GPCP version 2.1. Geophys. Res. Lett., 36, L17808. doi:10.1029/2009GL040000, 2009.

Huffman, G. J., Adler, R. F., Morrissey, M. M., Curtis, S., Joyce, R. J., McGavock, B., and Susskind, J.: Global precipitation at one-degree daily resolution from multi-satellite observations, J. Hydrometeor., 2, 36-50, doi: 10.1175/1525-7541(2001)002<0036:GPAODD>2.0.CO;2, 2001.

Huffman, G.J., Adler, R.F., Bolvin, D.T., Gu, G., Nelkin, E.J., Bowman, K.P., Hong, Y., Stocker, E. F., and Wolff, D. B.: The TRMM multisatellite precipitation analysis (TMPA): Quasi-global, multiyear, combined-sensor precipitation estimates at fine scales, J. Hydrometeor., 8(1), 38-55, doi: 10.1175/JHM560.1, 2007.

Hughes, D. A.: Comparison of satellite rainfall data with observations from gauging station networks, J. Hydrol, 327, 399-410, doi: 10.1016/j.jhydrol.2005.11.041, 2006.

Immerzeel, W. W., Rutten, M. M., and Droogers, P.: Spatial downscaling of TRMM precipitation using vegetative response on the Iberian Peninsula, Remote Sens. Environ., 113, 362-370, doi: org/10.1016/j.rse.2008.10.004, 2009.

Javanmard, S., Yatagai, A., Nodzu, M. I., BodaghJamali, J., and Kawamoto, H.: Comparing high-resolution gridded precipitation data with satellite rainfall estimates of TRMM_3B42 over Iran, Advances in Geosciences, 25, 119-125, doi: :10.5194/adgeo-25-119-2010, 2010.

Jia, S. F., Zhu,W. B., Lu, A. F., and Yan, T. T.: A statistical spatial downscaling algorithm of TRMM precipitation based on NDVI and DEM in the QaidamBasin of China, Remote Sens. Environ., 115, 3069-3079, doi: org/10.1016/j.rse.2011.06.009, 2011.

Joyce, R.J., Janowiak, J.E., Arkin, P.A., and Xie, P.: CMORPH: A method that produces global precipitation estimates from passive microwave and infrared data at high spatial and temporal resolution, J. Hydrometeor., 5(3), 487-503, doi: 10.1175/1525-7541(2004)005<0487:CAMTPG>2.0.CO;2, 2004.

Karl, T. R., Wang, W. C., Schlesinger, M. E., Knight, R. W., and Portman, D.: A method of relating general circulation model simulated climate to the observed local climate. part I: seasonal statistics, J. Climate, 3(10), 1053-1079, doi: 10.1175/1520-0442(1990)003<1053:AMORGC>2.0.CO;2 , 1990.

Kenabatho, P. K., Parida, B. P., and Moalafhi, D. B.: The value of large-scale climate variables in climate change assessment: The case of Botswana's rainfall, Physics & Chemistry of the Earth Parts, 50-52:64-71, doi: 10.1016/j.pce.2012.08.006, 2012.

Kidd, C. and Levizzani, V.: Status of satellite precipitation retrievals, Hydrol. Earth Syst. Sci., 15(4), 1109-1116, doi: 10.5194/hessd-7-8157-2010, 2011.

Kidd, C., Kniveton, D. R., Todd, M. C., and Bellerby, T. J.: Satellite rainfall estimation using combined passive microwave and infrared algorithms, J. Hydrometeor., 4(6), 1088, doi: 10.1175/1525-7541(2003)004<1088:SREUCP>2.0.CO;2, 2003.

Krajewski,W. F. and Smith, J. A.: Radar hydrology: rainfall estimation, Adv. water Resour., 25, 1387-1394, doi: 10.1016/S0309-1708(02)00062-3, 2002.

Kummerow, C., Hong, Y., Olson, W. S., Yang, S., Adler, R. F., Mccollum, J., Ferraro, R., Petty, G., Shin, D. B., and Wilheit, T. T.: The evolution of the goddard profiling algorithm (gprof) for rainfall estimation from passive microwave sensors, J. Appl. Meteorol, 40(11), 1801-1820, doi: 10.1175/1520-0450(2001)040<1801:TEOTGP>2.0.CO;2, 2001.

Ma, Y. Z., Liu, X. N., and Xu, S: The description of Chinese radiation data and their quality control procedures, Meteorol. Sci. 2, 53–56, 1998.

Magnusson, M., Vaskevicius, N., Stoyanov, T., Pathak, K., and Birk, A.: Beyond points: evaluating recent 3d scan-matching algorithms, 3631-3637, doi: 10.1109/ICRA.2015.7139703, 2015.

Mekonnen, G., Witold, F. K., Tomas, M. O., Yukarin, T., Phillip, A., and Katayama, M.: Scaling of tropical rainfall as observed by TRMM precipitation radar, Atmos. Res., 88, 337-354, doi: 10.1016/j.atmosres.2007.11.028, 2008.

Orlanski, I.: A rational division of scales for atmospheric processes, Bull. Amer. Meteor. Soc., 56, 527–530, 1975.

Prigent, C.: Precipitation retrieval from space: an overview. Comptes Rendus Geosciences, 342(4), 380-389, doi: 10.1016/j.crte.2010.01.004, 2010.

Rickenbach, T. M.: Convection in TOGA COARE: Horizontal Scale, Morphology, and Rainfall Production, J. Atmos. Sci., 55(17),2715-2729, doi: 10.1175/1520-0469(1998)055<2715:CITCHS>2.0.CO;2, 1998.

Romilly, T. G. and Gebremichael, M.: Evaluation of satellite rainfall estimates over ethiopian river basins, Hydrol. Earth Syst. Sci., 15(5), 1505-1514, doi: 10.5194/hess-15-1505-2011, 2011..

Schmidli, J., Frei, C., Vidale, P. L.: Downscaling from gcm precipitation: a benchmark for dynamical and statistical downscaling methods. Int. J. Climatol., 2006, 26(5), 679–689, doi: 10.1002/joc.1287.

Smith, E. A., Lamm, J. E., Adler, R., Alishouse, J., Aonashi, K., Barrett, E. C, Bear, W., Chang, A., et al.: Results of the WetNet PIP-2 Project. J. Atmos. Sci., 55, 1483-1536, doi: 10.1175/1520-0469(1998)055<1483:ROWPP>2.0.CO;2, 1998.

Sohn, B. J., Han, H. J., and Seo, E. K.: Validation of satellite-based high-resolution rainfall products over the korean peninsula using data from a dense rain gauge network, J. Appl. Meteorol. Clim., 49(2009), 367-70, doi: 10.1175/2009JAMC2266.1, 2010.

Thiemig, V., Rojas, R., Zambranobigiarini, M., Levizzani, V., and De Roo, A.: Validation of satellite-based precipitation products over sparsely gauged african river basins, J. Hydrometeor., 13(6), 1760-1783, doi: 10.1175/JHM-D-12-032.1, 2012.

Tobler, W.: On the first law of geography: A reply, Ann. Assoc. Amer. Geog., 94(2), 304-310, doi: org/10.1111/j.1467-8306.2004.09402009.x, 2004.

Trapp, R. J.: Mesoscale-convective processes in the atmosphere, Cambridge University Press, New York, USA, 346, 2013.

Turk, F. J. and Miller, S. D.: Toward improved characterization of remotely sensed precipitation regimes with modis/amsr-e blended data techniques, IEEE T. Geosci. Remote, 43(5), 1059-1069, doi: 10.1109/TGRS.2004.841627, 2005.

Ushio, T., Sasashige, K., Kubota, T., Shige, S., Okamoto, K., Aonashi, K., Inoue, T., Takahashi, N., and Iguchi, T., Kachi, M, Oki, R., Morimoto, T., and Kawasaki, Z. I.: A Kalman filter approach to the Global Satellite Mapping of Precipitation (GSMaP) from combined passive microwave and infrared radiometric data, J. Meteorol. Soc. Japan, 87, 137-151, doi: 10.2151/jmsj.87A.137, 2009.

Wigley, T. M. L., Jones, P. D., Briffa, K. R., and Smith, G.: Obtaining sub-grid-scale information from coarse-resolution general circulation model output, J. Geophys. Res. Atmos., 95(D2), 1943–1953, doi: 10.1029/JD095iD02p01943, 1990.

Wilby, R. L. and Wigley, T. M. L.: Downscaling general circulation model output: a review of methods and limitations, Prog. Phys. Geog., 21(4):530-548, doi: 10.1177/030913339702100403, 1997.

Wilby, R. L., Dawson, C. W., and Barrow, E. M.: Sdsm- a decision support tool for the assessment of regional climate change impacts, Environ. Modell. Softw., 17(2), 145-157, doi: org/10.1016/S1364-8152(01)00060-3, 2002.

Wilks, D. S.: Statistical Methods in the Atmospheric Science, Academic, San Diego, Calif, 465, 1995.

Willems, P. and Vrac, M.: Statistical precipitation downscaling for small-scale hydrological impact investigations of climate change, J. Hydrol., 402(402):193-205, doi: 10.1016/j.jhydrol.2011.02.030, 2011.

Table 1 Geographic and climatic situations of the six regions in China

Region	Longitude latitude	Elevation rang(m)	Annual Precipitation (mm)	Climate zone	
SE	110°E~115°E 23°N~28°N	22~1405	1230	Subtropical humid	Monsoon
CE	114°E~119°E 33°N~38°N	6~1533	670	Warm temperate semi-humid	Monsoon
NE	121°E~126°E 46°N~51°N	147~740	460	Mid temperate humid	Monsoon
CW	99°E~104°E 34°N~39°N	1368~8500	40	Warm temperate arid	Non-monsoon
NW	82°E~87°E 41°N~46°N	320~2458	70~140	Mid-temperate arid	Non-monsoon
TP	89°E~94°E 28°N~33°N	3552~8260	420	Temperature plateau	Non-monsoon

Table 2 Validation results of the daily precipitation for CMORPH and DCDF in 2014 in the six study regions.

Indexes	Time	Type	SE	CE	NE	CW	NW	TP
B(%)	1year	CMORPH	-29.60	-12.82	-7.09	-5.57	120.22	26.41
		DCDF	-3.91	11.54	15.85	32.82.	145.43	52.33
	SP	CMORPH	-20.82	-3.31	-45.50	45.44	159.02	83.32
		DCDF	-7.35	2.94	31.23	50.92	191.79	100.36
	SU	CMORPH	-22.12	3.17	6.78	-43.92	143.11	-9.49
		DCDF	-10.47	2.66	5.94	25.91	217.04	7.53
	FA	CMORPH	-57.75	-33.00	-16.90	10.90	114.44	43.22
		DCDF	5.92	33.95	19.88	25.78	128.51	59.77
	WI	CMORPH	-94.19	-32.83	-96.20	1042	-73.75	1655
		DCDF	10.35	20.54	22.39	1874	54.58	2106
RMSE	1year	CMORPH	12.20	6.69	6.71	3.85	2.32	4.50
		DCDF	7.94	4.38	5.16	4.74	3.96	6.08
	SP	CMORPH	16.23	4.79	3.13	2.81	2.41	2.70
		DCDF	11.81	7.32	2.77	2.80	3.09	3.45
	SU	CMORPH	16.61	10.25	12.39	5.74	3.38	7.43
		DCDF	13.83	10.95	10.64	6.98	5.13	10.27
	FA	CMORPH	6.14	6.90	3.89	3.93	1.94	3.46
		DCDF	0.19	6.44	2.67	4.51	3.72	3.98
	WI	CMORPH	3.80	1.59	0.68	1.61	0.65	2.45
		DCDF	2.86	2.05	0.41	2.47	1.14	3.49
CC	1year	CMORPH	0.52	0.32	0.32	0.17	0.33	0.28
		DCDF	0.60	0.47	0.42	0.29	0.29	0.33
	SP	CMORPH	0.59	0.34	0.36	0.17	0.07	0.04
		DCDF	0.66	0.40	0.38	0.17	0.05	0.04
	SU	CMORPH	0.36	0.19	0.25	0.17	0.40	0.23
		DCDF	0.48	0.26	0.46	0.44	0.44	0.37
	FA	CMORPH	0.40	0.50	0.36	0.07	0.32	0.11
		DCDF	0.52	0.53	0.46	0.10	0.21	0.08
	WI	CMORPH	0.31	0.02	0.00	0.05	0.03	0.06
		DCDF	0.52	0.17	0.05	0.01	0.02	0.15
POD	1year	CMORPH	0.64	0.59	0.51	0.76	0.52	0.80
		DCDF	0.77	0.74	0.62	0.80	0.69	0.87
	SP	CMORPH	0.68	0.52	0.45	0.82	0.51	0.70
		DCDF	0.80	0.66	0.60	0.95	0.63	0.72
	SU	CMORPH	0.86	0.69	0.78	0.82	0.80	0.91
		DCDF	0.99	0.85	0.91	0.87	0.90	1.00
	FA	CMORPH	0.50	0.67	0.46	0.71	0.80	0.72

		DCDF	0.65	0.75	0.59	0.84	0.92	0.89
	WI	CMORPH	0.22	0.19	0.00	0.28	0.59	0.14
		DCDF	1.00	1.00	1.00	1.00	1.00	1.00
FAR	1year	CMORPH	0.30	0.63	0.48	0.65	0.76	0.65
		DCDF	0.35	0.59	0.55	0.72	0.81	0.64
	SP	CMORPH	0.17	0.76	0.63	0.71	0.85	0.78
		DCDF	0.21	0.70	0.73	0.81	0.92	0.85
	SU	CMORPH	0.31	0.53	0.36	0.33	0.68	0.30
		DCDF	0.43	0.52	0.41	0.57	0.79	0.38
	FA	CMORPH	0.46	0.52	0.58	0.69	0.68	0.73
		DCDF	0.48	0.58	0.66	0.89	0.66	0.91
	WI	CMORPH	0.54	0.90	1.00	0.96	0.76	0.99
		DCDF	0.61	0.95	1.00	1.00	0.97	1.00
HSS	1year	CMORPH	0.43	0.25	0.34	0.08	0.14	0.13
		DCDF	0.39	0.31	0.35	0.14	0.08	0.09
	SP	CMORPH	0.41	0.13	0.23	0.00	0.09	0.01
		DCDF	0.44	0.21	0.29	0.03	0.11	0.07
	SU	CMORPH	0.38	0.29	0.40	0.25	0.17	0.22
		DCDF	0.32	0.35	0.37	0.33	-0.08	0.16
	FA	CMORPH	0.38	0.39	0.27	-0.02	0.17	0.04
		DCDF	0.39	0.48	0.34	0.01	-0.06	0.01
	WI	CMORPH	0.14	0.00	-0.01	-0.06	0.16	-0.06
		DCDF	0.21	0.07	0.03	-0.11	0.29	-0.16

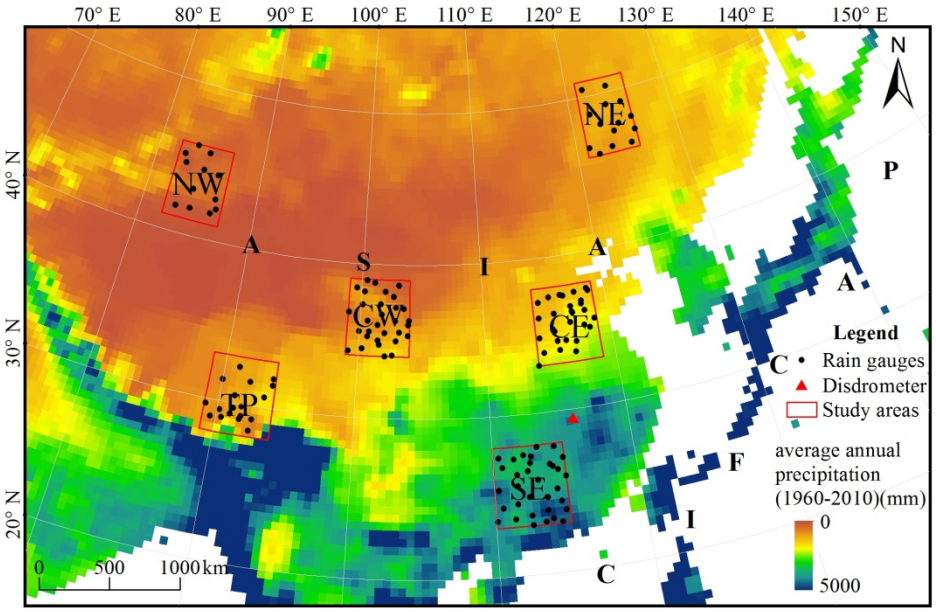

Fig. 1. Geographic and climate situations of the six regions. The locations of the rain gauges are superimposed

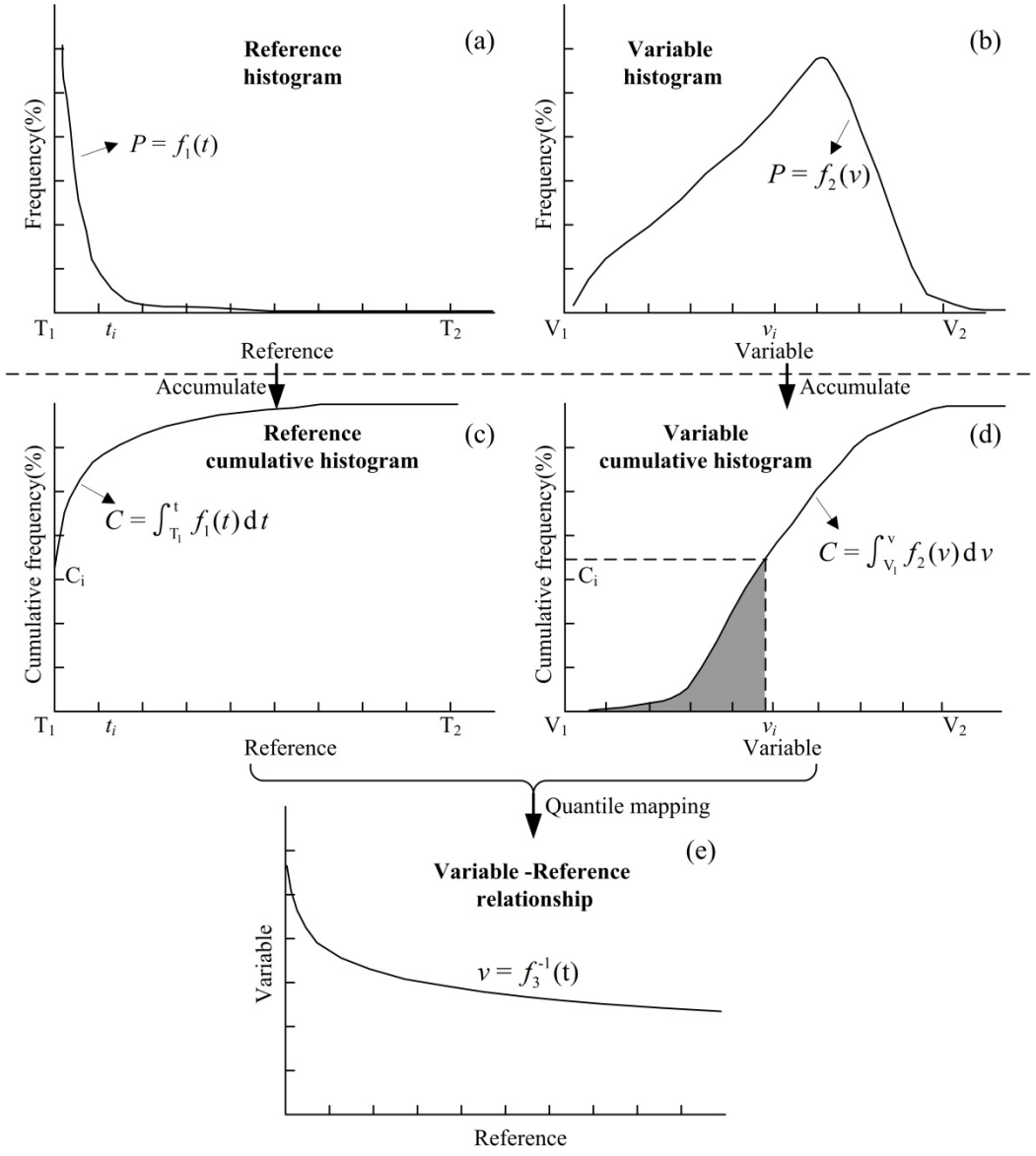

Fig. 2. Schematic of the cumulative distribution of frequency (CDF) matching method

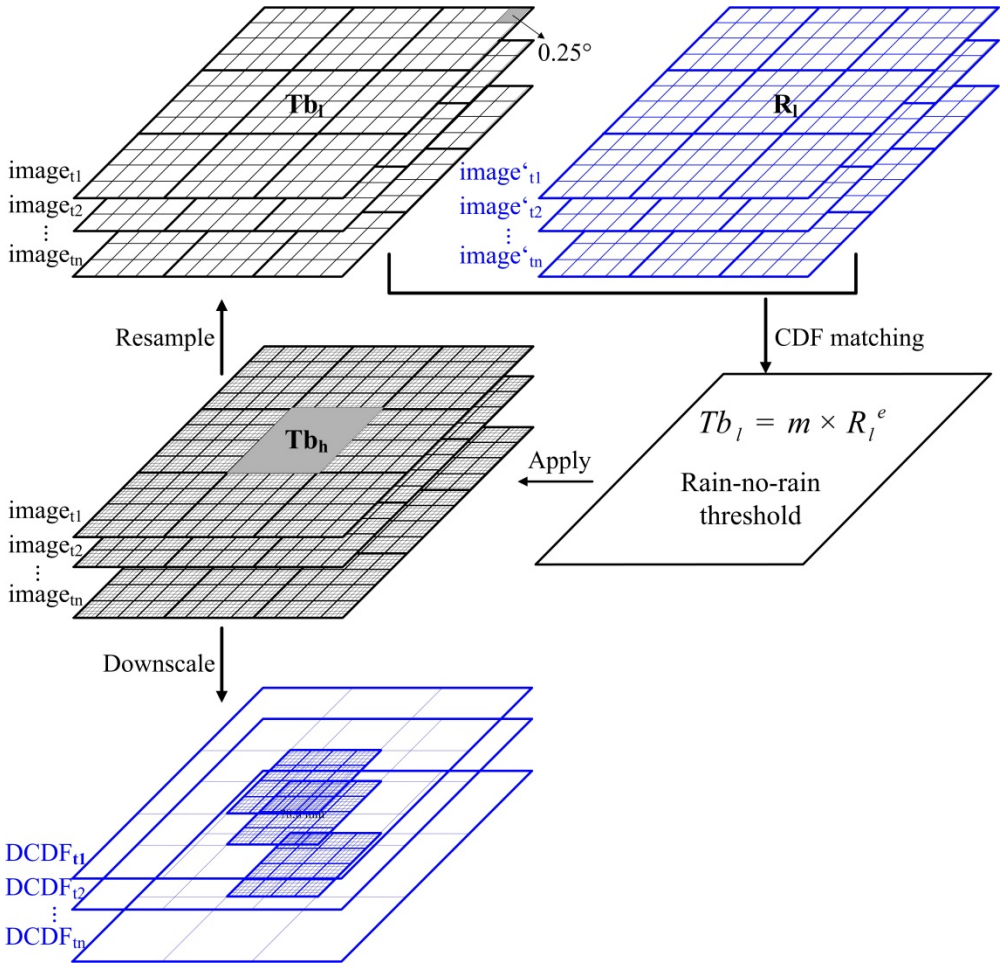

Fig. 3. Schematic of the CDF-based downscaling method (DCDF) using CMORPH and FY2-E Tb in this study. R represents precipitation rate.

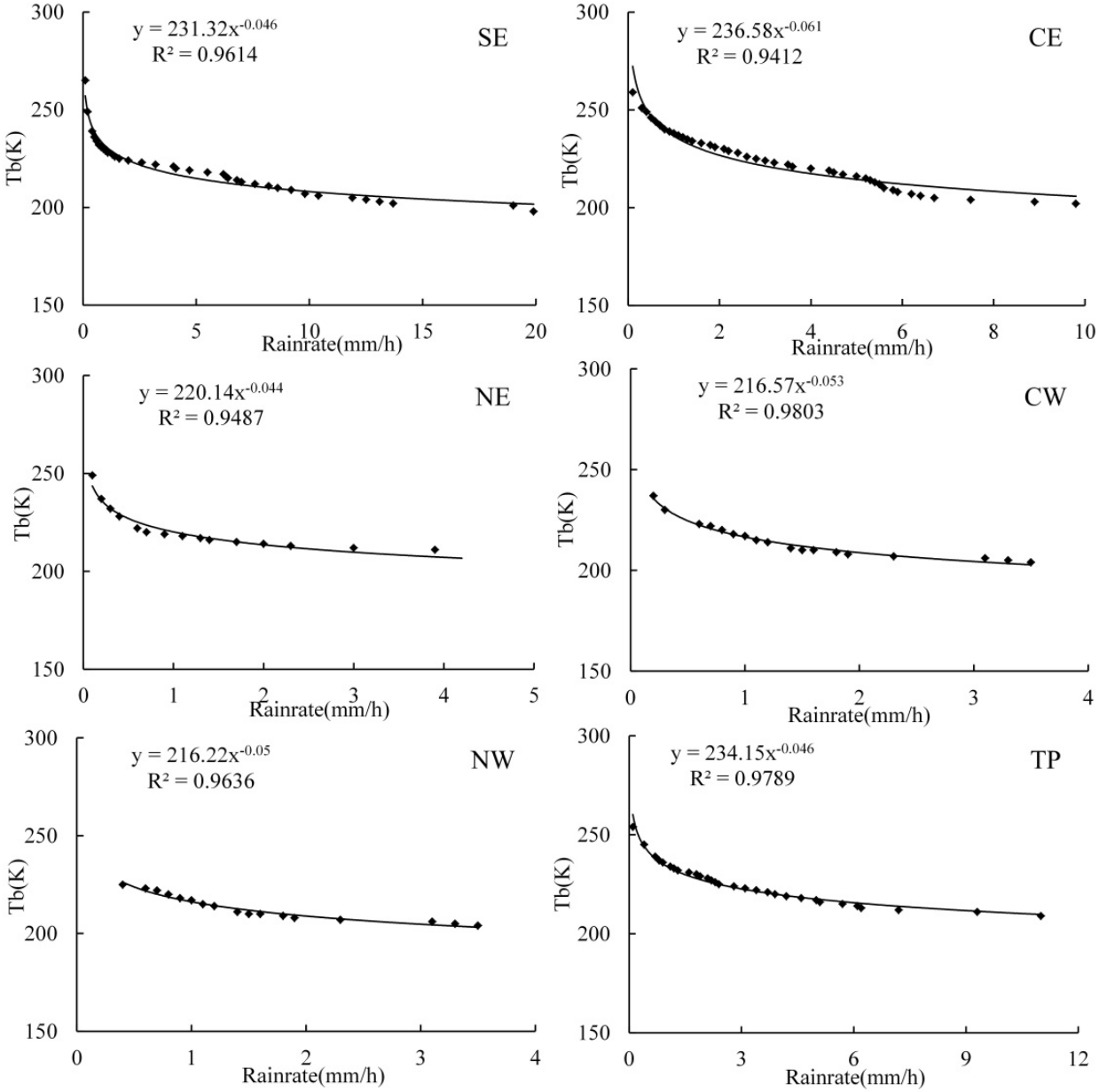

Fig. 4. Examples of fitting of precipitation rate and Tb for each region in China during 20140709-20140718 for subregion SE (115°35′E, 27°28′N), subregion CE (115°39′E, 36°14′N), subregion NE (124°20′E, 51°42′N), subregion CW (101°38′E, 37°31′N), subregion NW (85°43′E, 46°47′N), and subregion TP (91°06′E, 30°29′N).

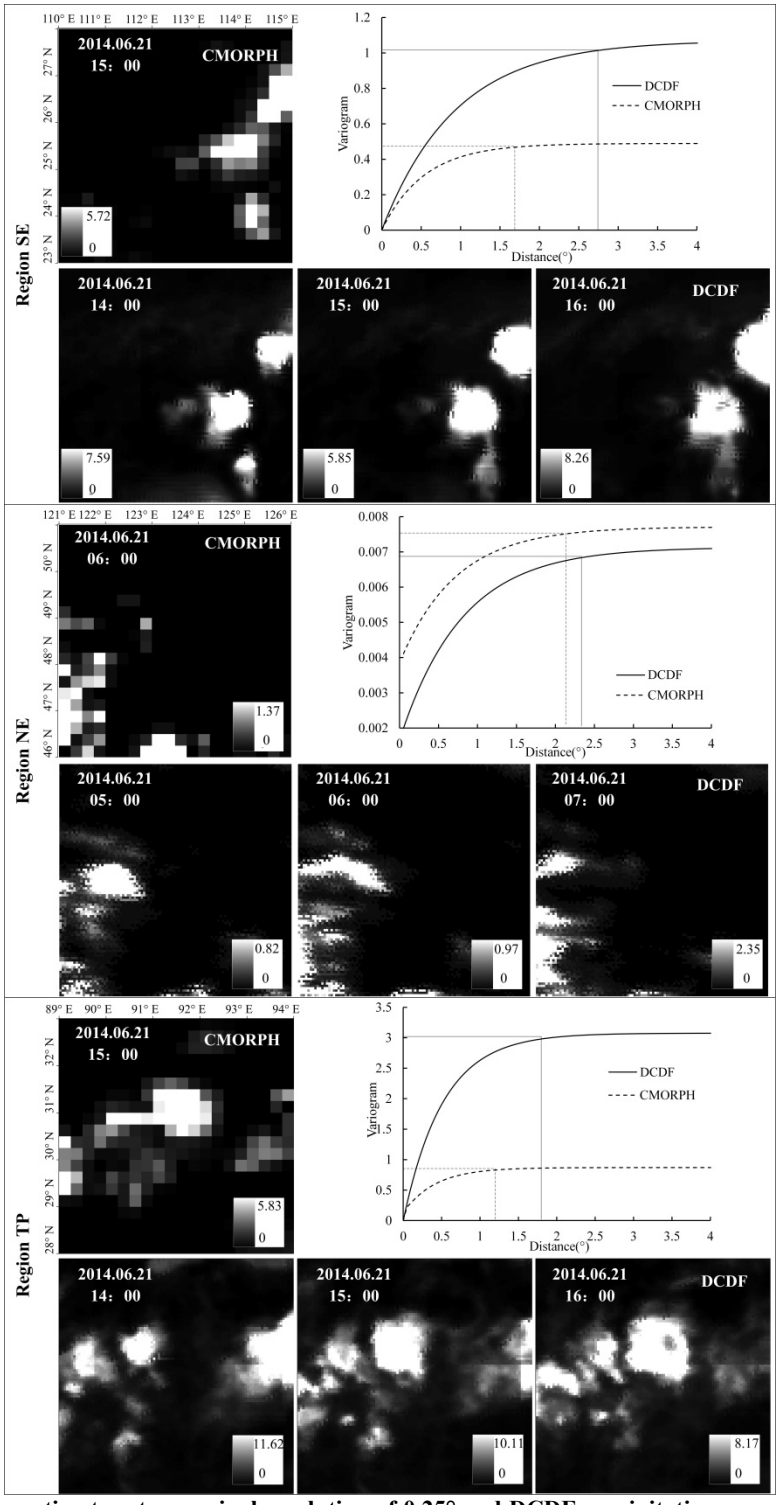

Fig. 5. CMORPH precipitation estimates at a nominal resolution of 0.25° and DCDF precipitation maps at a 0.05° resolution for regions SE, NE and TP

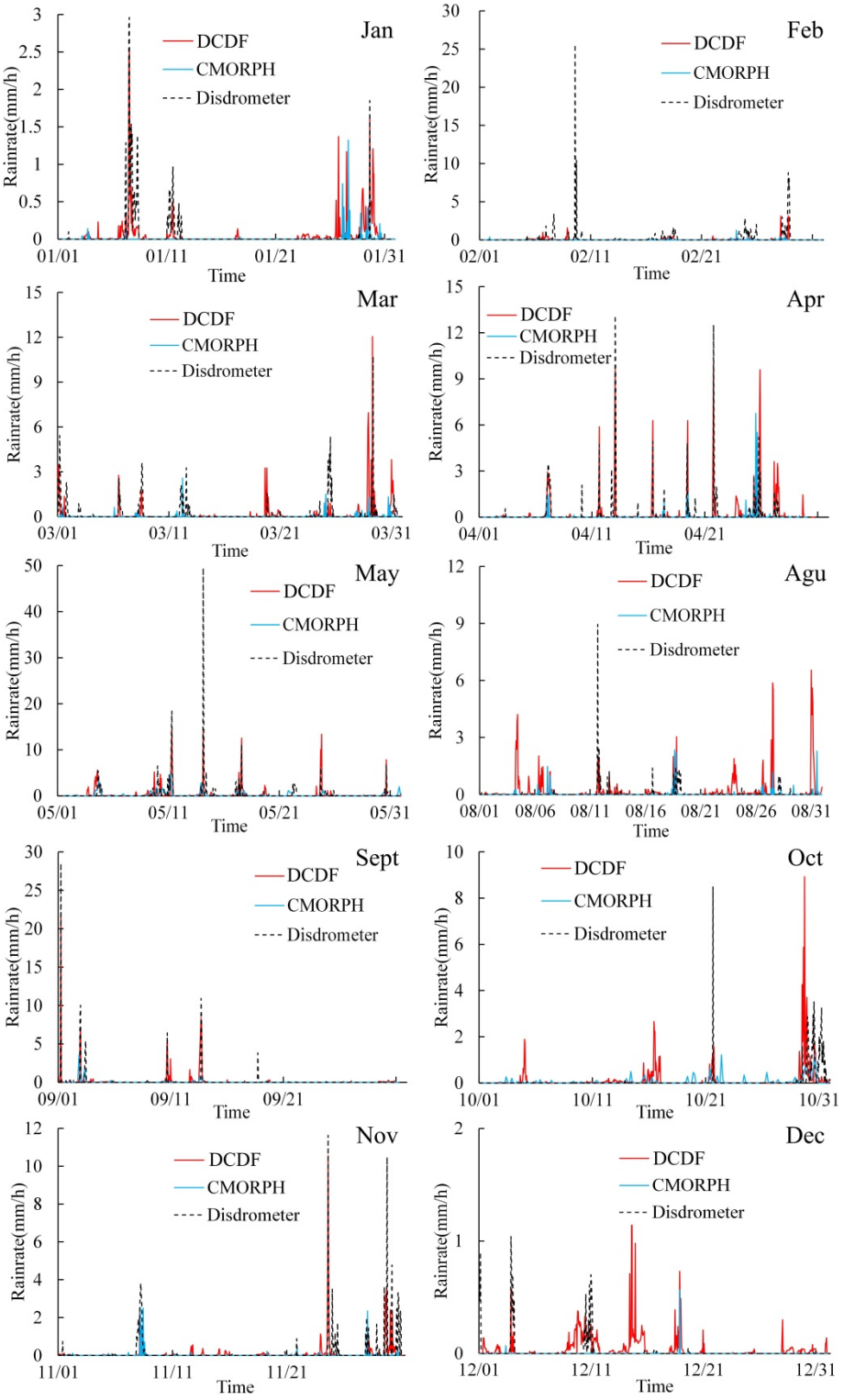

Fig. 6. Time series of disdrometer data, original CMORPH and DCDF precipitation at hourly scale in 2014

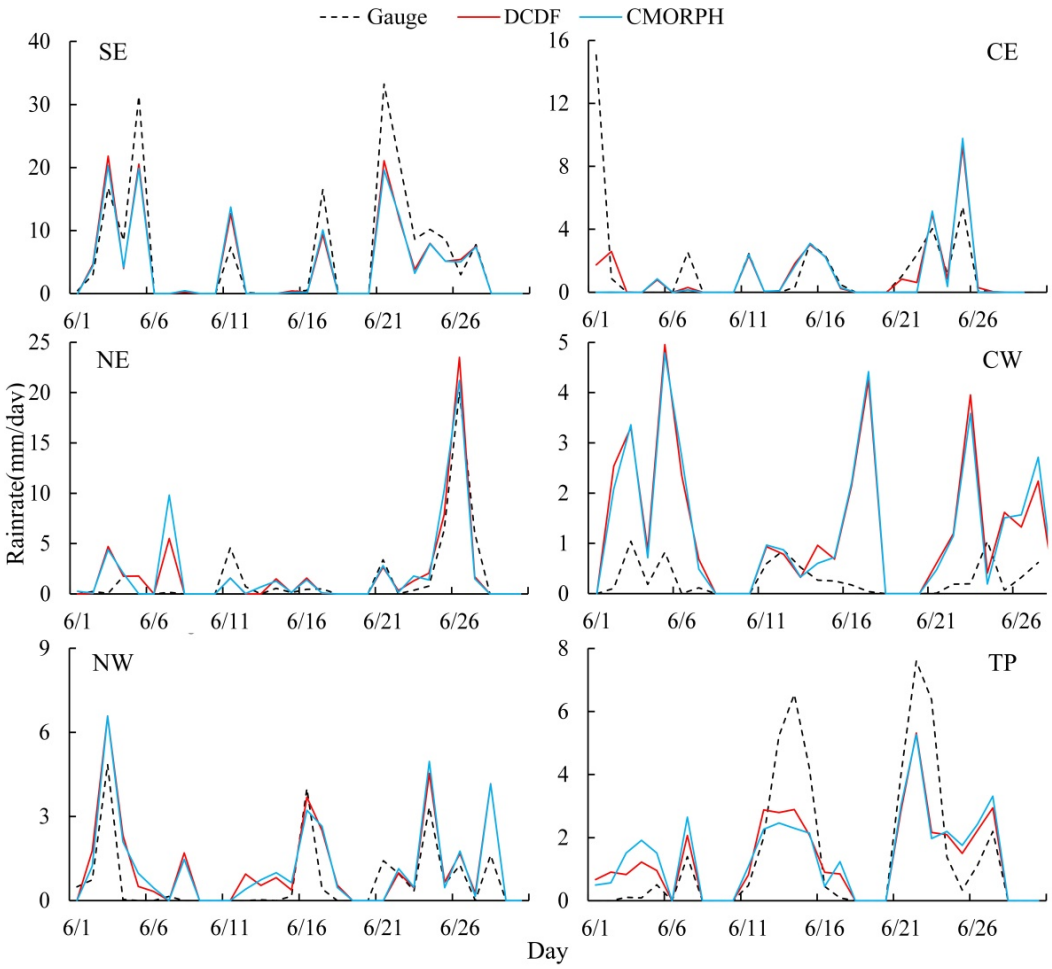

Fig. 7. Time series of the average precipitation of each region derived from gauge, DCDF and CMORPH at the daily scale in June 2014.

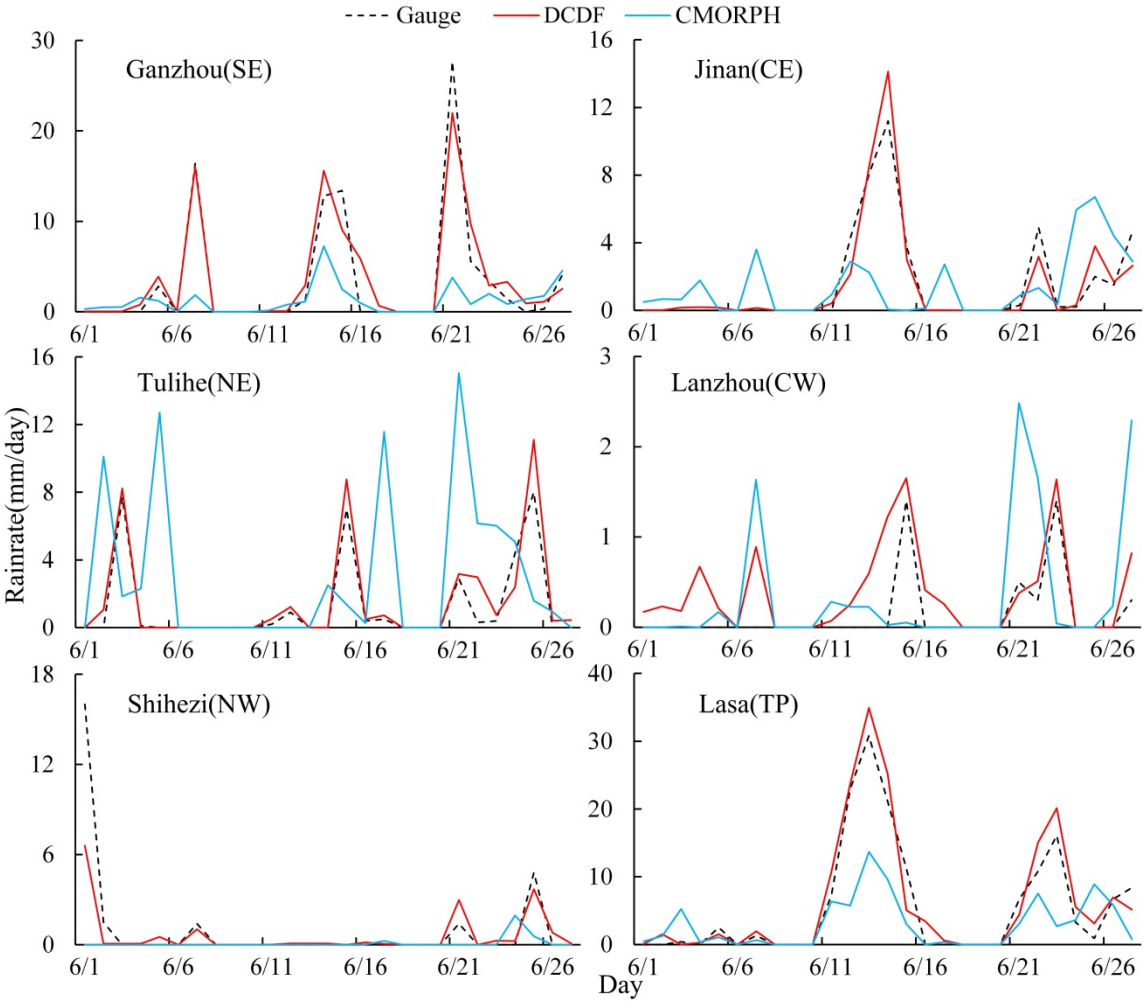

Fig. 8. Time series of rain gauge data, original CMORPH and DCDF precipitation for each randomly selected gauge. Ganzhou station (SE), 113.1667°E, 25.8667°N; Jinan station (CE), 117.05°E, 36.6°N; Tulihe station (NE), 121.6833°E, 50.4833°N; Lanzhou station (CW), 103.8833°E, 36.05°N; (e) Shihezi station (NW), 86.05°E, 44.3167°N; (f) Lasa station (TP), 91.1333°E, 29.6667°N.